ARIADNE

ARIADNE - A Novel Optical LArTPC: Technical Design Report and Initial Characterisation using the CERN T9 Testbeam and Cosmic Muons

UNIVERSITY OF
LIVERPOOL

ARIADNE - A Novel Optical LArTPC: Technical Design Report and Initial Characterisation using the CERN T9 Testbeam and Cosmic Muons
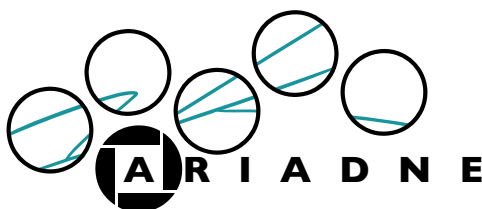
D. Hollywood, K. Majumdar, K. Mavrokoridis,[1] **K. J. McCormick, B. Philippou, S. Powell, A. Roberts, N. A. Smith, G. Stavrakis, C. Touramanis, and J. Vann**

University of Liverpool, Department of Physics, Oliver Lodge Bld, Oxford Street,
Liverpool, L69 7ZE, UK

E-mail: k.mavrokoridis@liv.ac.uk

ABSTRACT:

ARIADNE is a 1-ton two-phase liquid argon (LAr) time projection chamber (TPC) featuring a novel optical readout. Four electron-multiplying charge-coupled device (EMCCD) cameras are mounted externally, and these capture the secondary scintillation light produced in the holes of a thick electron gas multiplier (THGEM). Track reconstruction using this novel readout approach is demonstrated. Optical readout has the potential to be a cost effective alternative to charge readout in future LArTPCs.

In this paper, the technical design of the detector is detailed. Results of mixed particle detection at the CERN T9 testbeam (representing the first ever optical images of argon interactions in a two-phase LArTPC at a beamline) and cosmic muon detection at the University of Liverpool are also presented.

KEYWORDS: Time projection Chambers (TPC), Noble liquid detectors, Micropattern gaseous detectors, Photon detectors for UV, visible and IR photons (solid-state).

---

[1]Corresponding author

Contents

1 Introduction

1.1 The ARIADNE Experiment

Colossal scale Liquid Argon Time Projection Chambers (LArTPCs) will soon become a reality. In the neutrino sector, the DUNE project [1] is proposing the use of four 17,000 ton LArTPCs, while in the dark matter sector, DarkSide [2] is proposing the use of a 20 tonne two-phase LArTPC for direct dark matter detection. The cost and complexity of these large scale detectors means that early R&D work has the potential for a large return on investment.

ARIADNE is a 1-ton two-phase LArTPC, built to pursue the initial demonstration of optical readout [3, 4] on a larger scale. ARIADNE also serves as a platform for further R&D and the maturation of optical readout - a method which presents an alternative approach to the current paradigm of charge readout, offering the possibility of massive simplification and savings in construction and operation costs.

The ARIADNE TPC is 54 x 54 cm (x, y) with a total drift length of 80 cm (z). Four PMTs are installed below the TPC, providing detector triggering via the detection of primary scintillation (S1) light, and also performing auxiliary detection of secondary scintillation (S2) light.

The field cage of the TPC is composed of a total of 79 field-shaping rings, spaced 1 cm apart. The high density of the rings ensures high drift field uniformity. The cathode is installed at the base of the TPC, and can be biased up to 80 kV, providing a drift field of up to 1 kV/cm in the TPC. This bias is provided by a custom high-voltage feedthrough, described in more detail in Section 2.2. Above the field cage is an extraction grid, and a Thick Gas Electron Multiplier (THGEM) is placed 11 mm above the extraction grid. Both segmented and monolithic THGEM designs have been used on ARIADNE - these are detailed in Section 2.3. The space between the extraction grid and THGEM forms the extraction region, which is nominally biased with an extraction field of 4 kV/cm.

For the purposes of optical readout, a glass plate, with a coating of Tetraphenyl Butadiene (TPB) on its underside, is placed 2 mm above the THGEM. This plate shifts the 128 nm Vacuum Ultra Violet (VUV) light that is produced in the THGEM holes to 420 nm, allowing the EMCCD cameras and PMTs to operate close to their peak quantum efficiencies. Four EMCCD cameras, installed outside of the cryostat, look down at the THGEM through optical viewports and capture the S2 light produced in the THGEM holes.

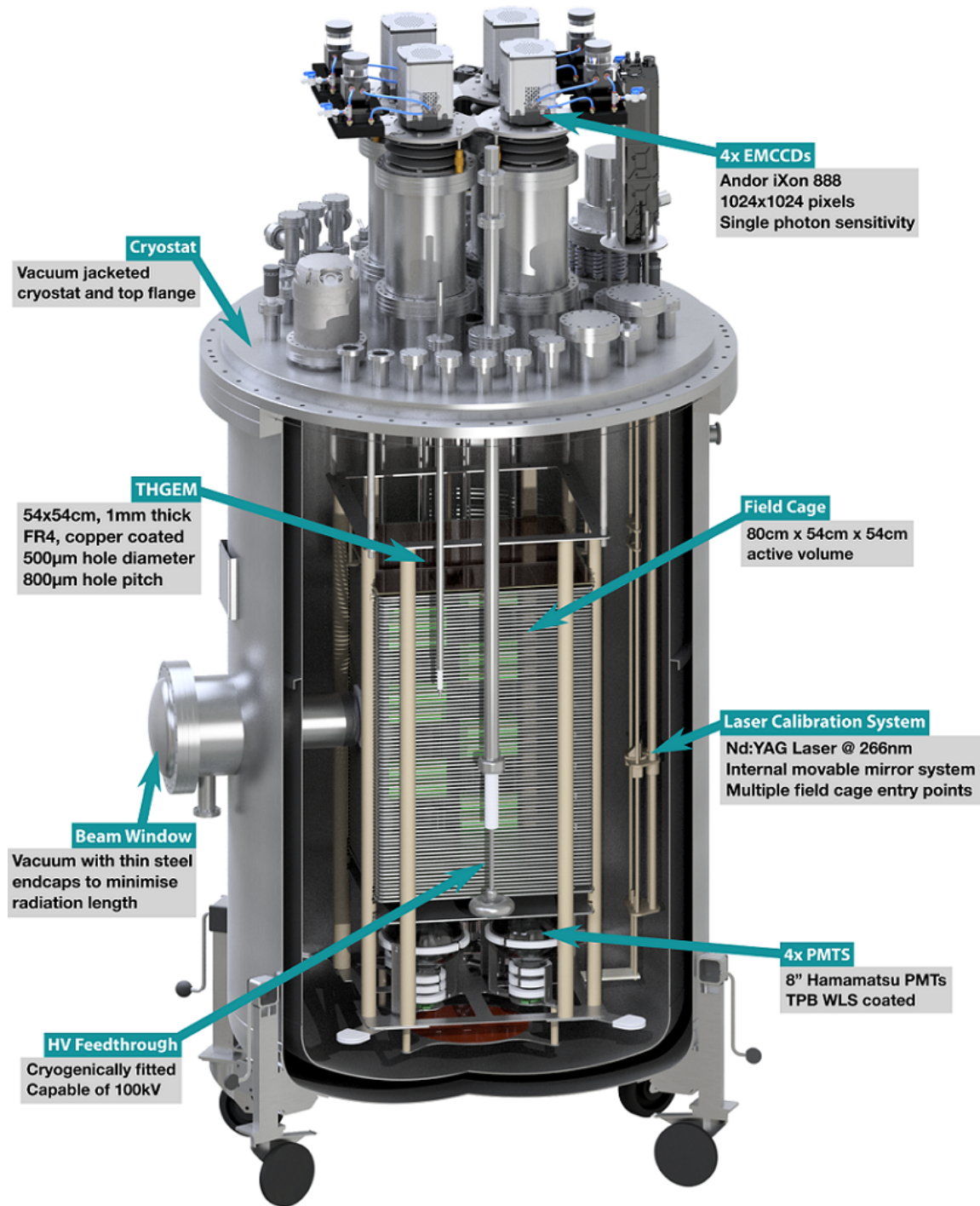Figure 1 shows a general overview of the ARIADNE detector.

4x EMCCDs
Andor iXon 888
1024x1024 pixels
Single photon sensitivity

Cryostat
Vacuum jacketed
cryostat and top flange

THGEM
54x54cm, 1mm thick
FR4, copper coated
500µm hole diameter
800µm hole pitch

Field Cage
80cm x 54cm x 54cm
active volume

Laser Calibration System
Nd:YAG Laser @ 266nm
Internal movable mirror system
Multiple field cage entry points

Beam Window
Vacuum with thin steel
endcaps to minimise
radiation length

4x PMTS
8" Hamamatsu PMTs
TPB WLS coated

HV Feedthrough
Cryogenically fitted
Capable of 100kV

Figure 1: The ARIADNE detector. The TPC is housed inside a vacuum-jacketed cryostat. A beam window and beam plug can be seen on the left of the image, penetrating through the cryostat walls and towards the TPC. Four EMCCD cameras are installed on the top flange, looking down into the cryogenic volume through viewports.

1.2 Detection Principle

Figure 2 shows a schematic of the detection principle of ARIADNE.

As a charged particle passes through LAr, it causes both ionisation and excitation of the argon atoms. The excited argon atoms emit primary scintillation (S1) light at 128 nm as they de-excite, which is immediately detected by the PMTs at the base of the TPC, and used as the event trigger. The electrons that were freed during ionisation are drifted towards the THGEM by the nominal 0.5 kV/cm drift field in the TPC. Once at the surface of the liquid, the electrons are extracted into the gas phase, and then directed into the THGEM holes, where they experience the much larger electric field - nominally on the order of 30 kV/cm - across the THGEM. This field is large enough to accelerate each electron above the scintillation threshold of gaseous argon - the electrons gain enough energy to excite the gas argon atoms that they collide with, resulting in the production of secondary scintillation (S2) light. The EMCCD cameras capture this S2 light, and reproduce a two-dimensional image of the ionising event in the TPC.

Traditionally, the S2 light produced in the THGEM would be captured using only PMTs, but this gives very limited information about the underlying structure of the light production. By instead capturing this light using EMCCD cameras, ARIADNE retains the positional information of the S2 light, with a nominal resolution of 1.1 mm per EMCCD sensor pixel. Events in the TPC are therefore reconstructed purely optically, with the high resolution of the EMCCD sensors providing high granularity tracking, and their single photon sensitivity allowing for optimisation of detection thresholds.
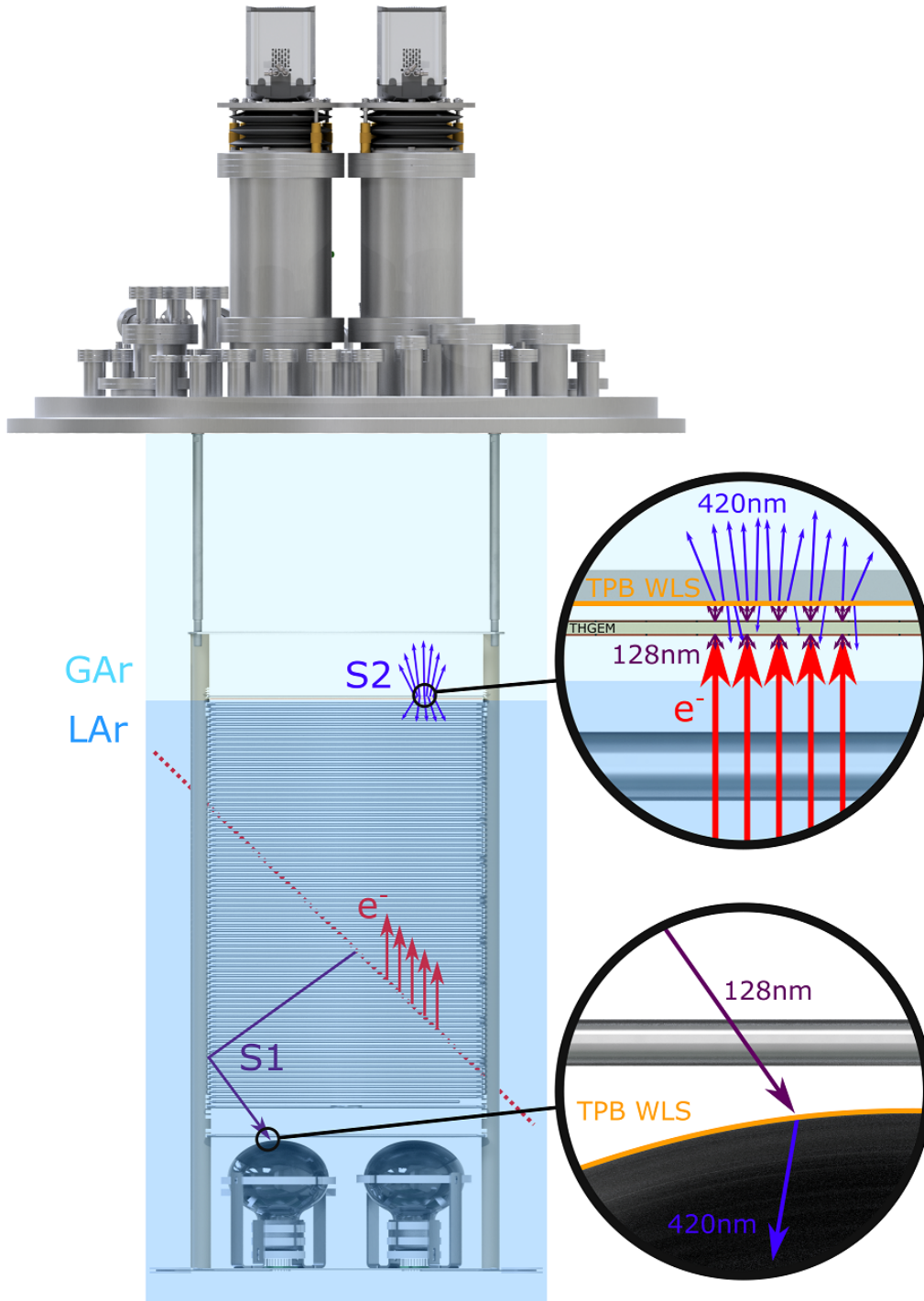
Figure 2: The detection principle of ARIADNE. An ionising track in the detector creates free electrons in the liquid argon, and the drift field in the TPC directs these electrons up towards the THGEM. The electrons are extracted out of the liquid phase and into the THGEM holes by the extraction field. Once inside a THGEM hole, the electrons are accelerated by the large electric field across the THGEM, and S2 light is produced by electroluminescence during this process. This S2 light is detected by the external EMCCD cameras.

2   Detector Design

2.1   TPC and Drift Field

Figure 3 shows an overall view of the ARIADNE TPC, with various surrounding detector components also shown for context.
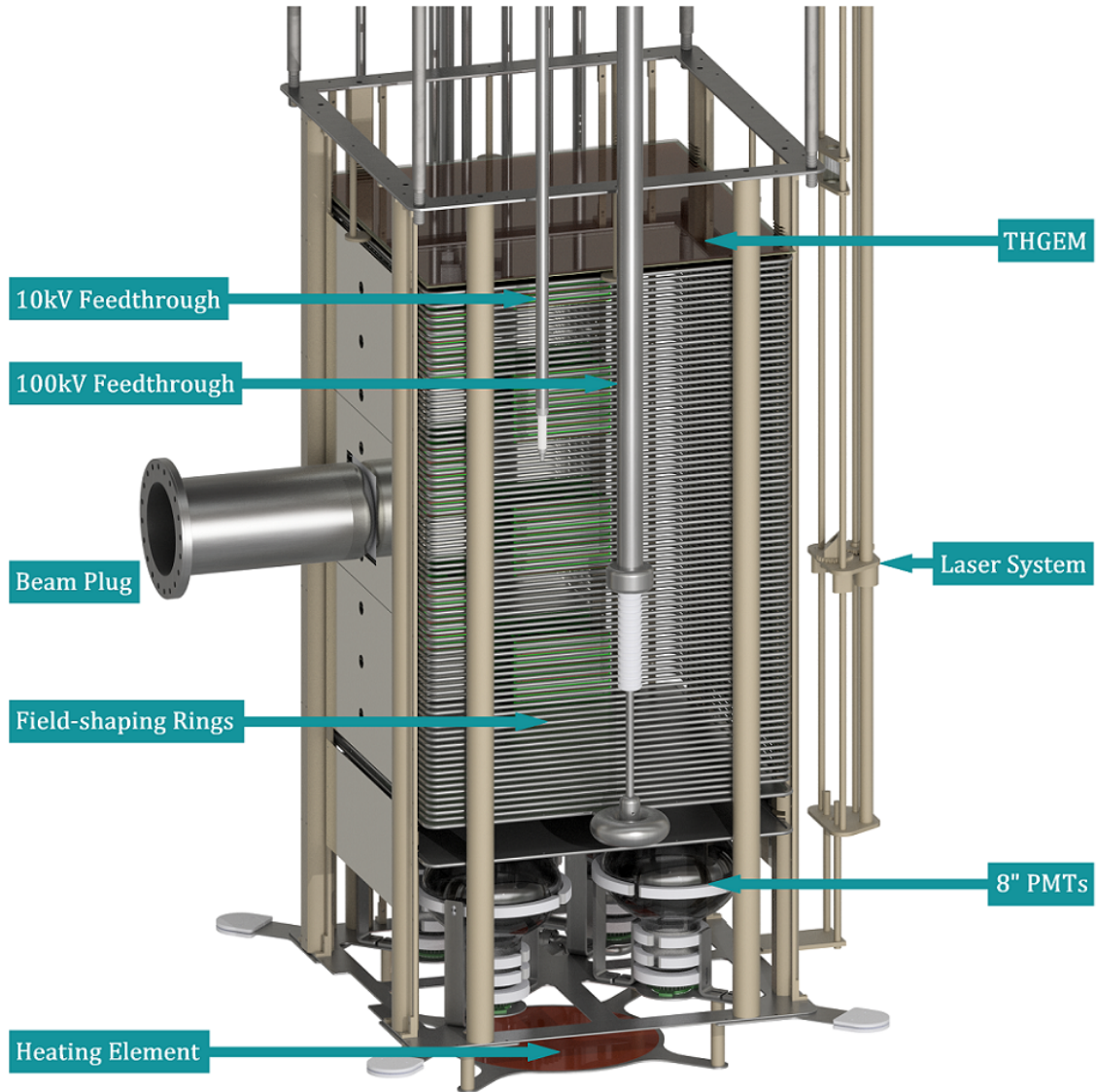

Figure 3: The ARIADNE TPC, with surrounding detector components also highlighted.

The field cage is defined by 79 CNC-bent stainless steel field-shaping rings. The ends of these rings are welded together and polished smooth, so as to not create sharp surfaces which may result in areas of locally high electric field. The cage is supported by 8 VICTREX® PEEK 450G rods, which have slots machined at regular intervals to support the field-shaping rings (one per slot). The rings have a vertical (centre-to-centre) spacing of 1 cm, giving a total TPC drift length of 80 cm, in-

cluding the spacing between the top ring and the extraction grid, and the bottom ring and the cathode.

The uniform gradient of the drift field is produced by a resistor chain - a series of 100 MΩ resistors connecting pairs of adjacent field-shaping rings, as well as connecting the extraction and cathode grids to the top and bottom rings respectively. The chain therefore dictates the resistance - and the voltage difference - between one ring and the next. A schematic of the connections between rings is shown in Figure 4.

As well as the fixed-value resistors, the chain also includes metal-oxide varistors, which are used for limiting the effects of any transients or voltage spikes, which would otherwise create a large potential difference between two or more rings, leading to a large current through - and potential damage to - the fixed-value resistors, or even parts of the detector itself. The varistors prevent this from occurring by effectively acting as a short-circuit above 1800 V, providing a safer circuit route to discharge the field cage, and so protecting the fixed-value resistors and detector from damage.
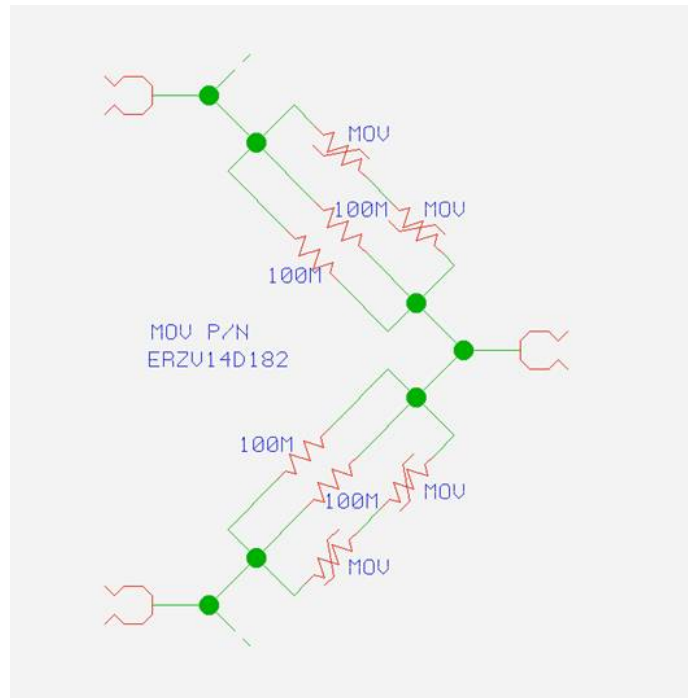

Figure 4: Schematic of the resistor chain connections and components between three adjacent field-shaping rings. The fuse clips at top-left, bottom-left and middle-right connect to the rings, and between each pair of clips are two 100 MΩ resistors in parallel, giving a total of 50 MΩ resistance between rings. In parallel with this are the metal-oxide varistors (all labelled as "MOV") for transient/surge protection.

The resistors are grouped onto 9 modules, one of which is shown in Figure 5. Each module consists of two PCBs: the first, which sits closest to the field-shaping rings, houses the resistors and varistors, and the second shapes the electric field around the first PCB and reduces its impact on the field uniformity within the TPC. It does this using embedded copper strips sitting parallel to - and biased

at the same voltage as - the field-shaping rings.

Each module houses 11 fuse clips for connecting to the field-shaping rings (1 per clip). The middle 7 rings are uniquely connected to each module, with the two top-most and bottom-most rings also being connected to the modules above and below respectively. The top 9 clips of each module are coupled to resistors as in Figure 4, but to ensure that the resistances of the overlapping rings remain consistent, the bottom 2 clips are not, instead acting as purely passive structural support. The clips are located on extensions to the first PCB layer, which can flex slightly to account for any small non-uniform contraction between the different materials present under cryogenic conditions, and therefore keep a consistent and tight connection to each ring. The modules are fitted to the inside of the field cage, in order to avoid introducing localised high electric fields outside the TPC.
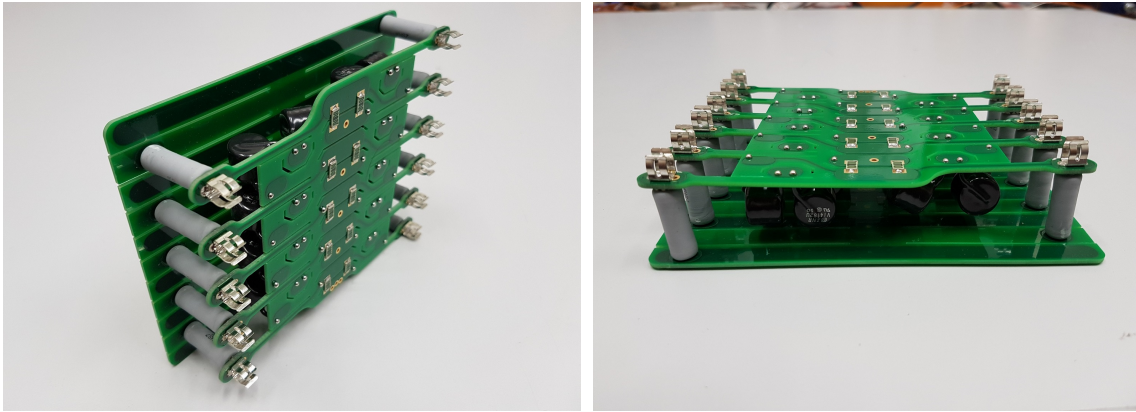

Figure 5: One of the resistor chain modules, which covers 9 unique field-shaping rings. The two PCBs can be seen, with the first housing the surface-mounted resistors and varistors, and the second acting as a field shaper. The fuse clips for connecting the module to the field-shaping rings are located on the flexible extensions to the first PCB.

Under normal operating conditions, the drift field has a nominal gradient of 0.5 kV/cm, but it is designed for operation up to 1 kV/cm. The uniformity of the drift field was optimised during the design phase of the experiment using COMSOL™ [5] simulations of the TPC - these are shown in Figure 6.

At and near the centre of the TPC, deviations from a uniform drift field are lower than 1%. These non-uniformities increase up to a level of $\approx 10\%$ approaching the outermost edges of the field cage, with localised deviations of up to 15% existing in the regions closest to the beam plug (discussed in Section 2.7) and the gaps in the field-shaping rings for the laser calibration system (discussed in Section 2.6). However, these deviations from uniformity are outside - and therefore do not affect - the (instrumented) active volume, which has an $x - y$ area of 53×53 cm as defined by the THGEM - i.e. slightly smaller than the 54×54 cm $x - y$ area of the field cage.
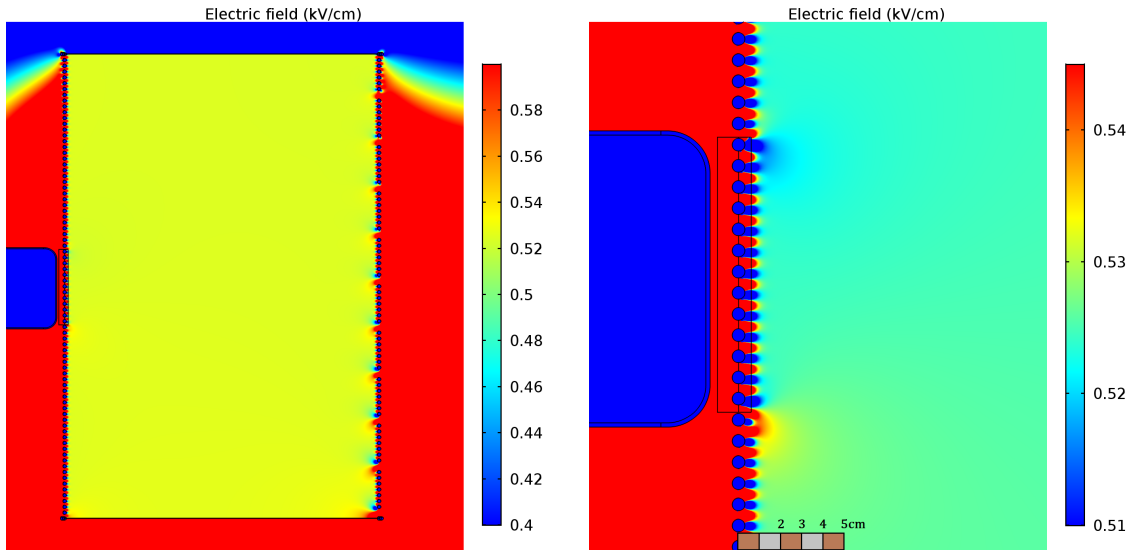
Figure 6: The results of COMSOL drift field simulations for the entire field cage (left) and the region within the field cage close to the beam plug (right). Small localised deviations from drift field uniformity of up to 15% exist in the region near the beam plug, but all non-uniformities subside to a level of no more than 1 % beyond a distance of ≈ 2 cm inwards from the field-shaping rings, as indicated by the scale bar at the bottom.

Energy Containment

A series of GEANT4 simulations was performed to study the energy containment of the ARIADNE TPC.

The simulated geometry of the detector is shown in Figure 7: the LAr volumes both inside and outside the field cage were modelled, and a particle gun corresponding to the beamline position was used to generate particles, initially at a rate corresponding to single incident particles, i.e. with no pileup. Later iterations of the containment simulations included additions such as simulation of beam spills, and therefore pileup, and cosmic muons. As well as providing results for energy containment, the simulation framework has been used to create training data that can be utilised for development of Machine Learning reconstruction techniques (which are not discussed in this paper).

The results of the energy containment simulations are shown in Figure 8.

The general trend for each particle species is as expected for passage through LAr. At low momenta, the energy containment is relatively high - 60% for electrons and positrons at 0.6 GeV/c - but a small momentum increase results in a significant reduction in containment - with electron / positron containment dropping by 10% as the momentum increases by 0.4 GeV/c. However, the relation between containment and momentum shallows as the latter continues to increase - with electron / positron containment decreasing to 30% at 4.0 GeV/c, and by a further 10% as the momentum then doubles to 8.0 GeV/c. Muons and pions both exhibit a similar trend, but with an overall lower absolute energy containment due to their specific interaction rates, as do protons and anti-protons at high momenta. However, at low momenta, protons and anti-protons exhibit some
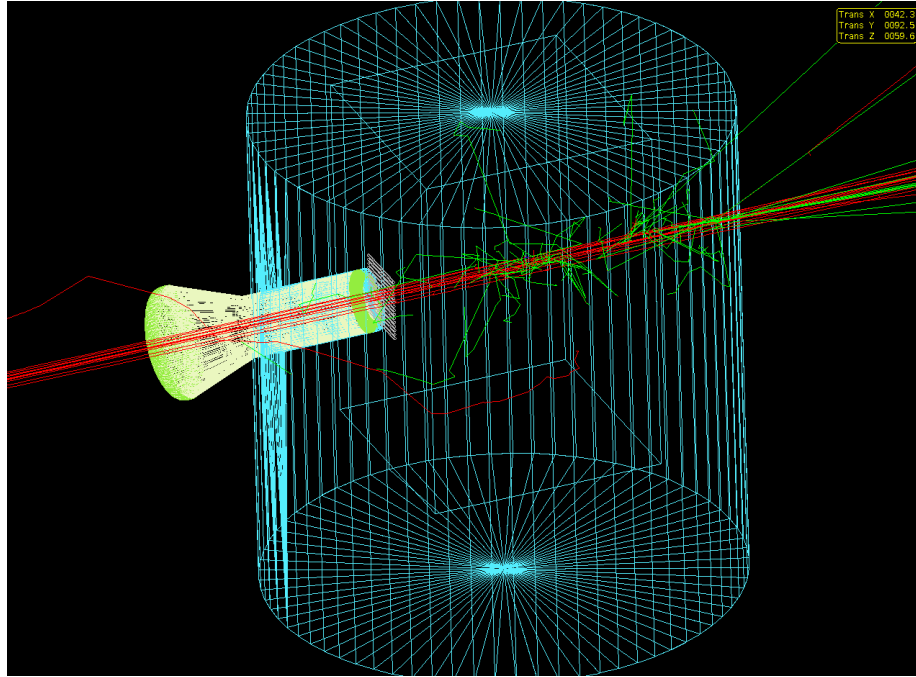
Figure 7: An example GEANT4 simulation of a spill of beam particles passing through the the ARIADNE detector (from left to right on the image). The LAr volume is shown in blue, with the beam plug (discussed in Section 2.7) shown in green. The grey box indicates the field cage.

Figure 8: The results of energy containment simulations, showing the fraction of each species of particle that is fully contained within the ARIADNE TPC at a given particle momentum. Per-point statistical uncertainties are comparable in size to the points displayed on the plot.

unique behaviour.
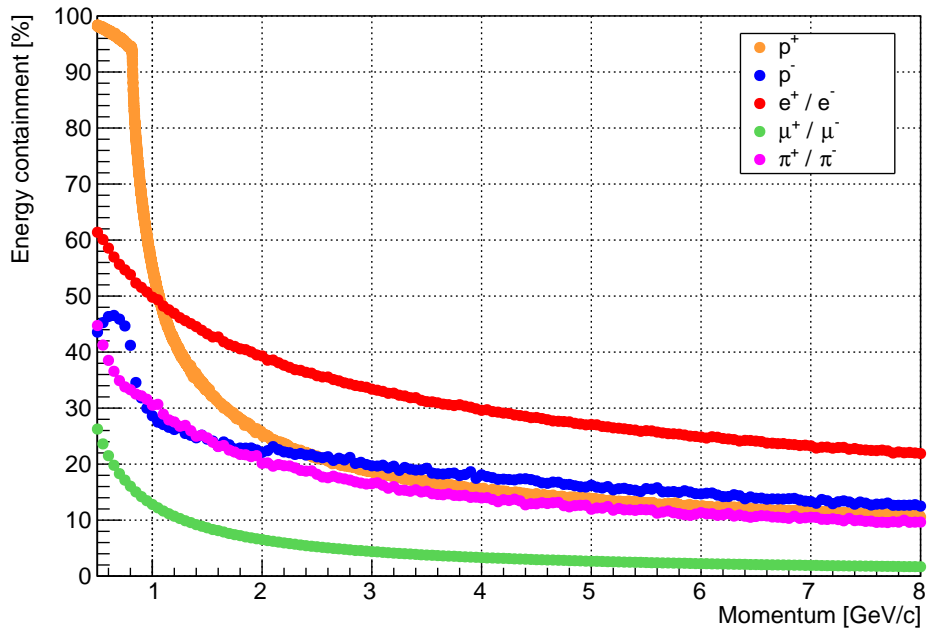
Low momentum protons are almost fully contained within the TPC, but show a very sharp drop in containment with a relatively small momentum increase between ≈ 0.8 and 2.0 GeV/c. This is due to the shape of proton tracks: they generally end in a very clear Bragg peak, where a large fraction of the energy is found. As the proton momentum increases, the interaction point moves further into the TPC, and beyond ≈ 0.8 GeV/c, it is located such that the Bragg peak is no longer within the active volume - it is lost, along with the large energy fraction it contains, resulting in the sudden decrease in energy containment.

Anti-proton interactions often result in products that travel both forwards (in the same direction as the incident anti-proton) and backwards (towards the source of the anti-proton). Low-momentum anti-protons will interact very close to the near edge of the active volume, resulting in the backwards-travelling products never entering the TPC, and therefore a reduced containment. For the case of passage through the ARIADNE detector, as the anti-proton momentum increases up to ≈ 0.5 GeV/c (the blue datapoints in Figure 8), the interaction point moves further into the active volume, with the backwards-travelling products being more contained within the TPC, and leading to the increase in containment seen in the simulation. Further momentum increase results in the forward-travelling interaction products beginning to escape from the other edge of the TPC, resulting in the sudden containment drop between ≈ 0.5 and 1.0 GeV/c.

These containment studies give an indication of the most useful momentum range over which the ARIADNE detector should be operated: from a lower limit of 0.5 GeV/c (in order to fully contain the low-momentum protons and anti-protons) to an upper limit of 8 GeV/c (beyond which the containment of the majority of particle species decreases below $\approx 10\%$). This momentum range was therefore used during operation at the CERN T9 Testbeam (discussed in Chapter 4).

2.2 Cathode and High Voltage Feedthrough

Positioned 1 cm below the bottom field-shaping ring, the ARIADNE cathode grid consists of a stainless steel frame containing a tensioned stainless steel mesh with 70% optical transparency. A 4.5 inch diameter field-shaping torus is welded to one side of the frame, and this is where the connection to the high voltage (HV) feedthrough is made. This torus shields the electric field where the HV connection is made, thus minimising corona effects. An external Heinzinger PNChp series 100 kV negative polarity power supply [6] provides the cathode bias.

Due to the high bias required on the cathode, the HV feedthrough of LArTPCs in general poses a significant engineering challenge. Care and attention is required to design and manufacture a feedthrough capable of providing both UHV leak tightness as well as discharge-free operation during extended periods of time in demanding cryogenic conditions.

The central core of the ARIADNE HV feedthrough makes connection with the cathode using a spring-loaded tip, which ensures a good electrical connection even if the cathode changes position slightly in cryogenic conditions. In order to make the feedthough vacuum tight, the central core is enclosed in a thick ultra-high-molecular-weight polyethylene (UHMWPE) jacket, which has been cryofitted onto the central core - creating a leak-tight seal through the cold flow of UHMWPE as it warms and compresses tightly against the central core.

To provide mechanical stiffness to the core assembly, the UHMWPE jacket is itself enclosed in a stainless steel jacket, which is grounded. This mechanical jacket extends from the Conflat flange on the air side of the feedthrough down to approximately 30 cm above the HV connection at the cathode. The large diameter of this outer stainless steel jacket provides substantial mechanical strength to the feedthrough, and its lower end terminates in a smaller, 68 mm diameter torus for field-shaping, thereby minimising the field between the central core and the end of the jacket.

The ARIADNE HV feedthrough has been successfully operated up to a bias of 80 kV, and is leak tight to better than 10^{-8} mbar l/s. Figures 9 and 10 show the feedthrough in isolation and in-situ on the TPC respectively, along with a cross section model of the feedthrough where it makes connection with the cathode torus. COMSOL simulations, shown in Figure 11, were performed to validate the design of the HV feedthrough as a whole.

Figure 9: The ARIADNE high voltage feedthrough. A 1 metre rule is shown for scale.

2.3 THGEM

A Thick Gaseous Electron Multiplier (THGEM) [7] is a type of gas micropattern detector, broadly consisting of two conducting copper planes separated by an insulating layer (typically made of FR4), with holes passing directly through all three layers. By applying an electric potential between the top and bottom planes of the THGEM, a strong electric field is created within each hole.

Depending on the bias that is applied across the THGEM, different regimes of operation are possible. At low bias, electrons that enter the THGEM holes will simply be drifted through and collect on the top plane. As the field increases, the incident electrons gain enough energy to overcome the scintillation threshold - that is, they have enough energy to excite gas argon atoms as they travel through the holes of the THGEM. When these excited argon atoms de-excite, they release photons with wavelengths centred around 128 nm - the peak scintillation wavelength of argon. This regime of operation is known as the electroluminescence regime. As the field across the THGEM continues to increase, the electrons may gain enough energy to ionise the gas argon atoms, liberating electrons which can themselves be accelerated and gain enough energy to liberate further electrons. The resulting electron avalanche is known as a Townsend discharge.

The ratio of the number of electrons leaving each hole to the number of incident electrons defines the gain of the THGEM.

Traditionally, high gain is required to overcome the noise of the THGEM readout electronics. However, when operating at a high gain, and if the number of incident electrons on the THGEM

Figure 10: (Left) The ARIADNE HV feedthrough in-situ on the TPC, with the spring-loaded tip sitting within the cathode grid torus. (Right) A cross section of the lower end of the HV feedthrough.

is large enough, it may be possible that sufficient ionisation occurs in a hole to form a plasma that is electrically conductive enough to induce a discharge between the top and bottom THGEM planes. This dependence of discharge probability on the incident electron population means that the operating bias of the THGEM must be carefully chosen: it should be high enough to give a good signal-to-noise ratio for low numbers of incident electrons, but low enough that a discharge is not induced during high intensity events which deposit large numbers of electrons.

Optical readout has the benefit of allowing the THGEM to operate in the electroluminescence regime, which - at a lower THGEM bias - is much more stable to variations in the number of incident electrons. However, optical readout still benefits from the exponential gain regime of the THGEM, as the ionisation also results in exponentially enhanced light production. Each incident electron can result in the production of many hundreds of photons, depending on the exact bias across the THGEM [8], and so optical readout may allow for improved detection thresholds compared to the collection of electrons (charge), as well as improved stability by allowing the THGEM to operate at a lower bias.

Two different THGEM designs, both built by the CERN PCB Workshop and shown in Figure 12, have been used in the ARIADNE detector: one in which the top plane has been segmented into 16 charge-independent pads (the "segmented" design), and one in which the top plane is a single entity (referred to as the "monolithic" design).
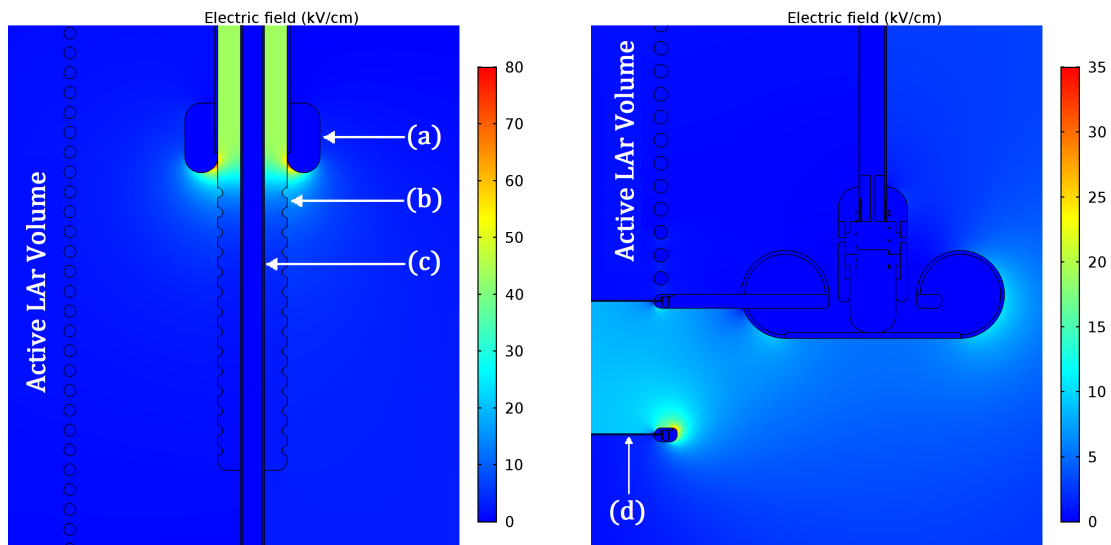
Figure 11: The results of COMSOL simulations of the HV feedthrough. (Left) A high electric field of 80 kV/cm is present at the field-shaping torus that terminates the feedthrough's grounded outer jacket (a), but the high dielectric strength of the inner UHMWPE jacket (b) prevents any discharges between the central core (c) and the outer jacket. (Right) The effectiveness of the torus surrounding the connection to the cathode is visible, with the largest field being 35 kV/cm, between the cathode and PMT protection (d) grids.
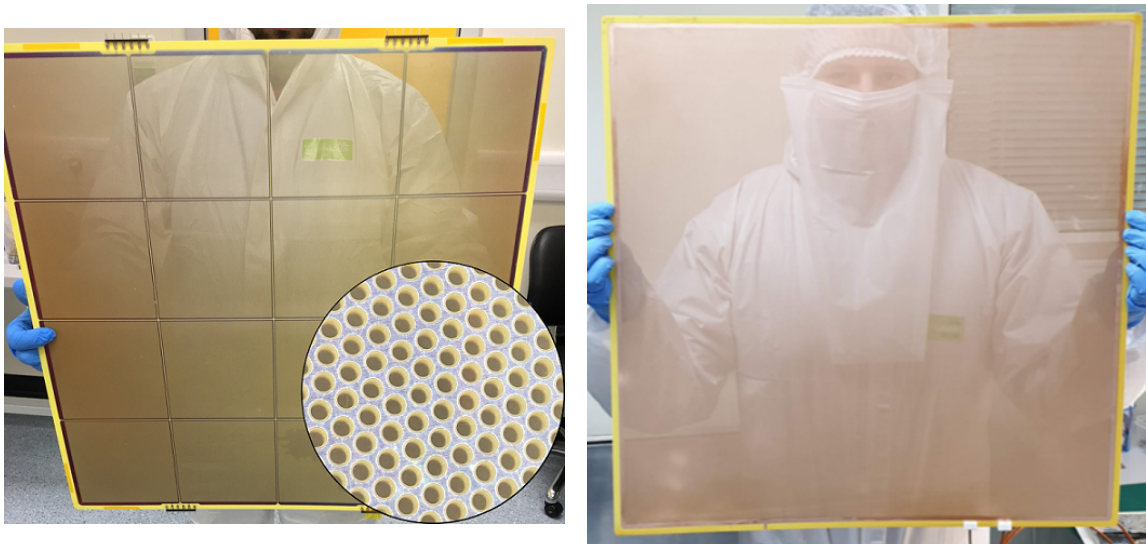

Figure 12: (Left) The 16-pad segmented ARIADNE THGEM. Inset: the THGEM hole structure (diameter: 500 μm, pitch: 800 μm). The 50 μm dielectric rim is visible around each hole. (Right) The monolithic ARIADNE THGEM. The hole structure and spacing is identical that of the segmented THGEM.

The two designs share a common underlying structure: a total area of 55.6×55.6 cm, with an active area (the area covered by holes) of 53×53 cm, and a total thickness of 1 mm. The holes have a diameter of 500 μm, with a 50 μm dielectric rim and 800 μm hole-to-hole pitch. The bottom plane of both designs is a single monolithic pad, with a single bias provided by a separate external HV supply to that used for the top plane.

When using the segmented THGEM, each of the pads is biased independently, but to the same potential, using an external pre-amp and bias distribution board. The pre-amp also collects the charge on each of the pads, at both high and low pre-amp gain values simultaneously, for a total of 32 charge readout channels. Two pre-amp gain values are used so as to utilise as much of the dynamic range of the digitiser being used to record the charge signal as possible across both small and large signals.

When using the monolithic THGEM, the top plane is biased and read out through a single external pre-amp.

The segmented THGEM was used for the beam studies conducted at the CERN T9 Testbeam (discussed in Chapter 4), while the monolithic design was used for cosmic muon studies at the University of Liverpool (discussed in Chapter 5).

2.4 PMTs and Light Collection

Argon emits scintillation light with a peak wavelength of 128 nm. However, the spectral response range of the Hamamatsu R5912-20 PMTs lies between 300 and 650 nm, with peak quantum efficiency at 420 nm [9], and the EMCCD cameras (discussed in more detail in Section 2.8) have a spectral response range between 300 and 1000 nm, with quantum efficiency of > 80 % between 420 and 780 nm, as shown in Figure 13. Therefore, since neither the PMTs nor the EMCCDs are directly sensitive to the VUV 128 nm photons, wavelength shifting is required.

As well as considerations relating to the emission spectrum of the wavelength shifter, it is necessary for it to be cryogenically stable. Tetraphenyl Butadiene (TPB) is an obvious choice in both regards, with its peak emission wavelength of 420 nm and an emission spectrum tail out to 550 nm, as shown in Figure 13. TPB has a successful history of use in many cryogenic LArTPC dark matter and neutrino experiments [12, 13].

In total, it was necessary to coat the four PMTs, the 54×54 cm wavelength shifting glass sheet positioned above the THGEM, and all of the 3M™ ESR (Enhanced Specular Reflector) Vikuiti™ polyester foil panels. These reflector panels surround the TPC, improving the light collection efficiency of the PMTs. The chosen method for this coating was vacuum evaporation, which produces a uniform, repeatable coating that ensures predictable wavelength shifting performance of the applied coatings.

When considering the TPB coating on the PMTs and glass, it is important to strike a balance between the TPB thickness and optical transparency: if the coating is too thick, then a photon which is absorbed by the TPB and re-emitted may not itself escape, but if the coating is too thin, the efficiency of shifting the 128 nm VUV photons is poor. The PMTs and glass plate were coated with a 0.05 mg/cm^2 layer, which was chosen based on various studies [13–15] which have demonstrated the response of PMTs to various TPB coating thicknesses. Optical transparency is not a concern for
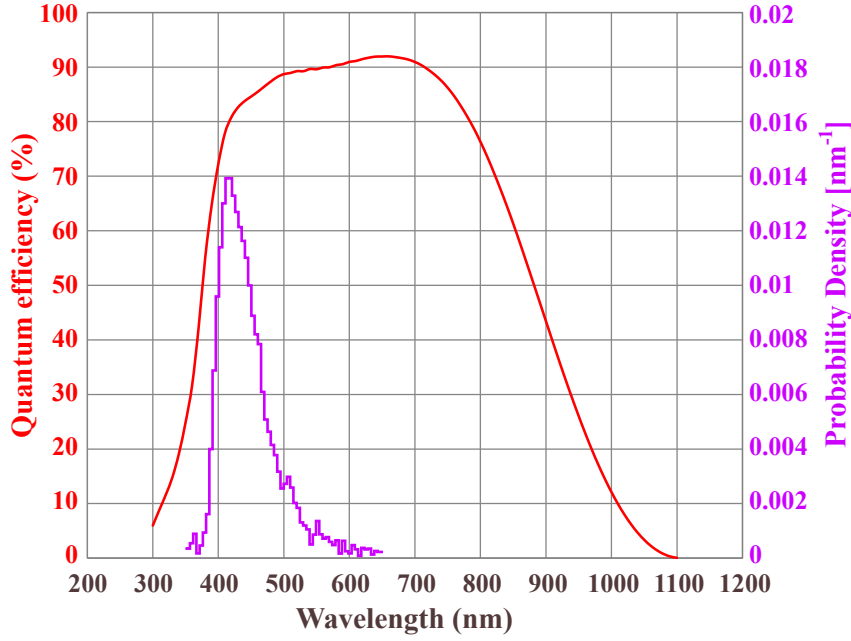
Figure 13: The emission spectrum of TPB (purple), with the the quantum efficiency of the EMCCD cameras (red) for comparison. This figure has been adapted from [10] and [11].

the reflectors, but instead, a balance is required between the increasing light collection efficiency and the increasing brittleness of the TPB coating as its thickness increases. A coating of 0.22 mg/cm^2 thickness was found to be a reasonable compromise.

A bespoke vacuum evaporation chamber - a model of which is shown in Figure 14 - was used for coating the listed ARIADNE components with TPB. During the coating procedure, the chamber was evacuated, and five crucibles (which hold the solid TPB powder) were slowly heated over a period of several hours, via a high current passed through copper blocks positioned underneath. The component(s) to be coated are suspended from a frame positioned above the crucibles, and the chamber as a whole is capable of coating a maximum single area of 60 × 60 cm. It is also equipped with a viewport, so that the coating process can be monitored. Figure 15 shows the PMTs, wavelength shifting glass sheet and reflector panels coated in TPB.

2.5 LAr Purification and Cryogenics

In order to most efficiently drift electrons the full 80 cm drift length of the TPC, it is desirable to maximise the electron lifetime, denoted by τ. This lifetime is heavily dependent on purity, and can be approximated as: τ [μs] $\approx 300 / \rho$, where ρ is the O$_2$ equivalent impurity concentration in parts per billion (ppb) [16, 17].

The fraction of electrons lost during drift by attachment to impurities is given by $Q = Q_0 e^{-t_{\text{drift}}/\tau}$, where Q is the number of electrons surviving a drift time t_{drift}, Q_0 is the initial number of ionised electrons and τ is the electron lifetime as before. When $\tau = t_{\text{drift}}$ only $\approx 27\%$ of electrons can be expected to survive. Given that the drift velocity of electrons in LAr is 1.5 mm/μs at the nominal ARIADNE drift field of 0.5 kV/cm [18], the maximum drift time is 530 μs - ap-

Figure 14: A model of the vacuum evaporation chamber, which was used to apply a TPB coating to the PMTs, the glass plate and the reflector panels. The five crucibles for holding the TPB powder can be seen at the bottom of the chamber, along with their associated copper blocks for heating and the frame for suspending the component(s) to be coated. The viewport is shown on the right of the image.

proximately corresponding to 0.6 ppb O_2 equivalent impurities in the detector volume. In practice, it is always preferable to have an electron lifetime longer than the maximum drift time, since the probability of an electron surviving the drift process is statistical, and the survival rate continues to be enhanced for τ much larger than t_{drift}. A lifetime of ≈ 5000 μs is required for 90% of electrons to survive drifting the full ARIADNE detector, and for 99% electron survival probability a lifetime of over 0.5 s is required.

The purity can also be measured by directly utilising the slow component of argon scintillation emission. This component - the characteristic decay time of which is denoted by τ_2 - is caused by the decay of triplet excimers (in contrast to the decay of singlet excimers, which produce the fast emission component with a decay time denoted by τ_1). The exact value of τ_2 is dependent on the source of the excitation, with measurements of 1540 ns (1100 ns) [19] and 1590 ns (1660 ns) [20] being reported in ultra-pure LAr for excitation via electrons (alpha particles). However, regardless
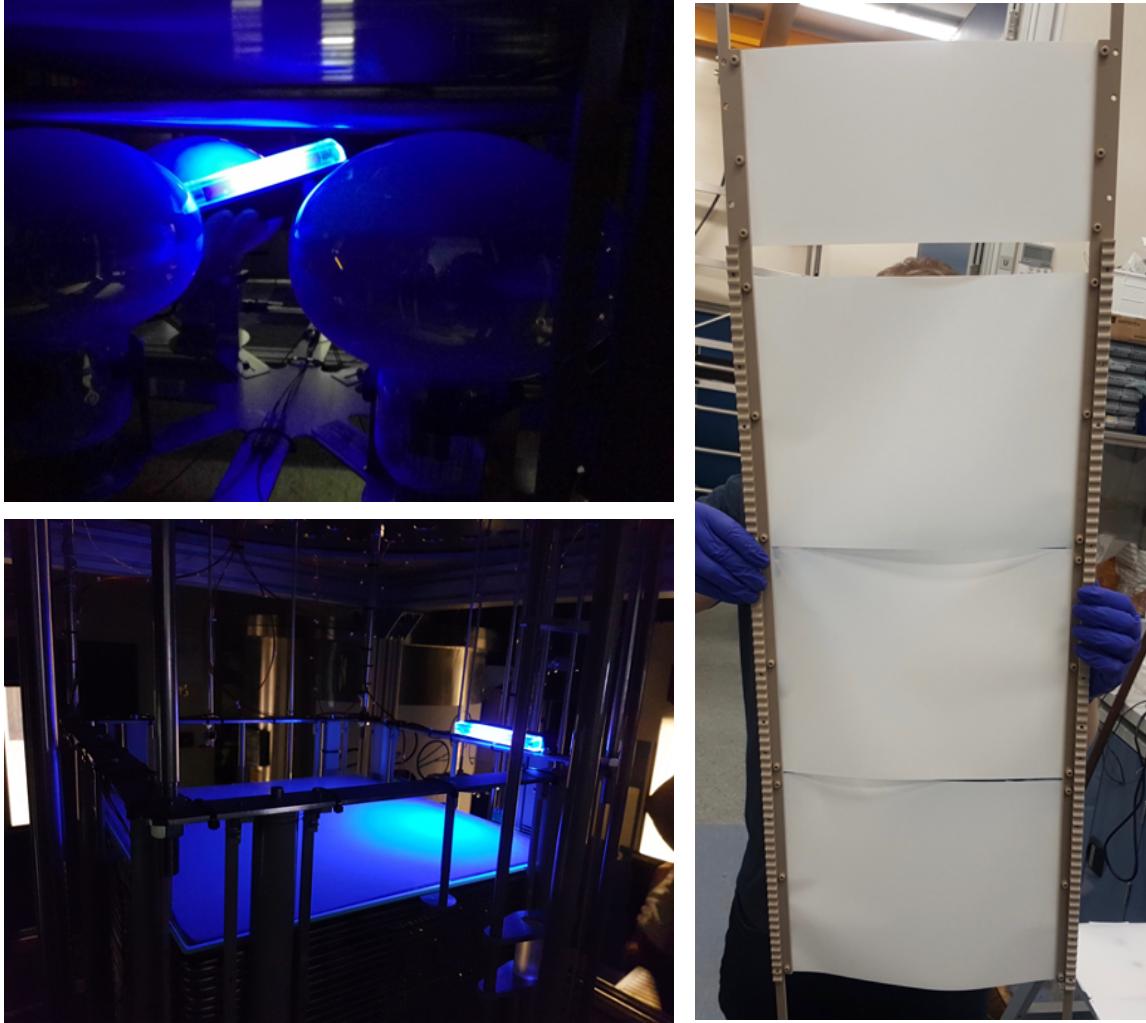
Figure 15: (Top-Left) The PMTs and (Bottom-Left) the glass sheet, viewed under UV light illumination to show the effect of the TPB coating. (Right) One of the TPC reflector assemblies after TPB coating.

of the excitation source, impurities in the argon can quench the production of triplet excimers more than that of singlet excimers [21], leading to a smaller slow emission component, and thus a τ_2 value smaller than the cited results.

The value of τ_2 is calculated by fitting a double-exponential function to the shape of S1 pulses recorded by a single PMT. The sensitivity of this method is limited to a few ppb equivalent impurity concentration [22], but it is still a useful tool during the initial stages of the purification process - particularly when the TPC is not fully submerged in LAr and application of a drift field is therefore not possible.

The combined internal recirculation and purification system has been generously sized in an attempt to ensure the best possible electron lifetimes even if the initial argon fill purity is poor.

The system is suspended from the underside of the top flange, and is completely submerged in

the LAr volume to minimise heat losses that may have otherwise been introduced with an external purification system. A bespoke positive displacement pump, designed and built by the authors specifically for ARIADNE, provides a nominal flow rate of 300 L/h through a 13.5 L filtration cartridge. This cartridge is filled with a mixture of Engelhard Cu-0226 S 14×20 Mesh (85.6%) working alongside 3 Å and 4 Å molecular sieves (both 7.2%), to provide efficient filtration of O_2 and H_2O impurities. A similar, smaller recirculation and purification system is described in [22].

The same mixture of chemicals is also present in a larger, 30 L external filtration cartridge, which provides initial purification of the LAr immediately after it leaves the supply dewar - this is shown in Figure 16. This extra purification step is not essential, but reduces the burden on the internal purification system.

Figure 16: The external 30 L filtration cartridge, showing the mixture of 85.6% Engelhard Cu-0226 S 14×20 (brown balls) and 7.2% of both 3 Å and 4 Å molecular sieves (white cylinders in two different sizes). The same mixture is present in the internal 13.5 L cartridge.

Figure 17 shows a schematic of the system that is used to fill, recirculate, purify and evacuate LAr to and from the ARIADNE detector.

The LAr is initially stored in a supply dewar, and passes into the external filtration cartridge via a inlet line controlled with two valves (V_{0A} and V_1). The LAr leaves the filtration cartridge (which is equipped with a 1.5 bar(g) safety relief valve), and enters the main detector volume via valves V_2 and V_3. This "liquid-in" line deposits the LAr at the bottom of the cryostat.

The cryostat is equipped with multiple pressure sensors (only one of which is shown in Figure 17 for clarity, and discussed in more detail in Section 3.1), a 0.6 bar(g) relief valve, and two exhaust lines for releasing excess pressure if required - these lines are independently controlled using valves V_7 and V_8. Gas can also be let into the detector volume via V_8.

During purification, LAr is drawn from the lowest part of the volume into the pump (shown by 'L_{in}' on Figure 17), and then passes into the internal filtration cartridge via valve V_6. This cartridge is equipped with check valves (rated to 10 mbar) that only allow one-way flow, and therefore ensure that there is no contamination of the chemicals within the cartridge when it is at atmospheric pressure. Once purified, the LAr then empties back into the detector at a sufficient distance from the L_{in} line to ensure well-distributed purity within the volume. An alternate route out of the pump - controlled by valves V_5 and V_4 - is used for pumping the LAr out of the cryostat.

The V_5 and V_6 valves are mutually exclusive - that is, when one is fully closed, the other is fully open. This is done via a gearing system that rotates the valves in opposite directions, with user control being provided by a single rotation feedthrough.
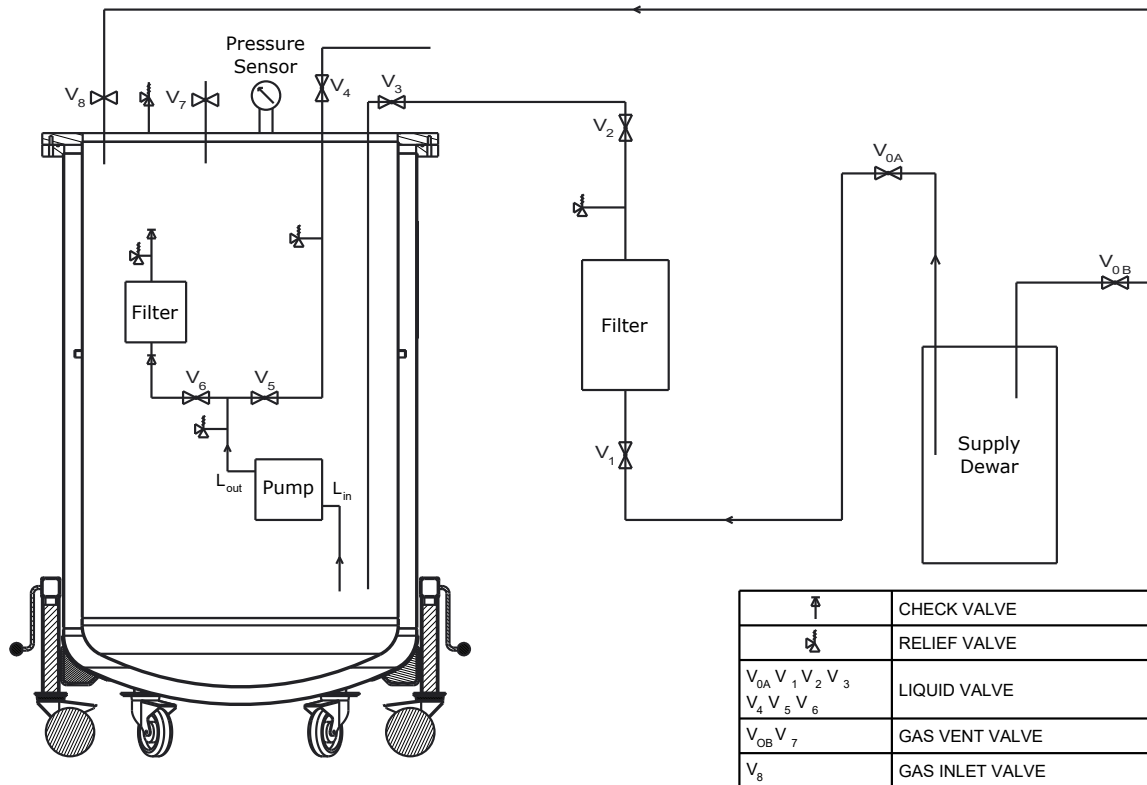

Figure 17: Schematic showing the various lines and valves used to fill, recirculate, purify and evacuate LAr to and from the ARIADNE detector. See main text for detailed explanation.

Figure 18 shows the progression of τ_2 - the decay time of the slow scintillation emission component - as a function of time during purification. The starting τ_2 value of ≈ 1160 ns relates directly to the initial LAr fill purity, and it can be seen that after only 20 hours of purification, τ_2 has plateaued at a value of 1350 ns. This is somewhat less than the reported values previously discussed, but may be attributed to the inefficiency of the purification system at removing N_2, which is a considered to be a light-quenching impurity, but has little effect on the electron lifetime. Further purification will therefore continue to remove O_2 contamination - thus increasing the electron lifetime - with little additional change in τ_2. For the results discussed in Sections 4.4 and 5.3, the electron lifetime was

$\approx 250~\mu s$, as determined from analysis of the PMT S2 pulses, corresponding to an impurity level of 1.2 ppb O_2 equivalent.
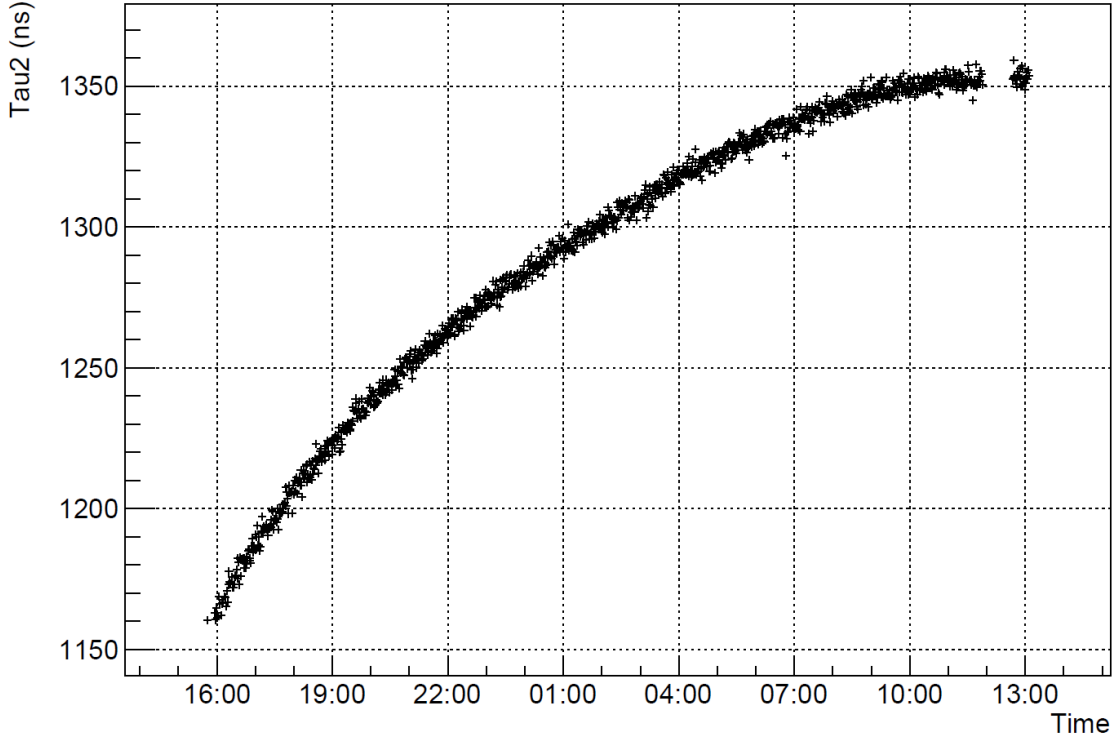

Figure 18: Progression of τ_2 - the decay time of the slow scintillation emission component - as a function of time during purification. The gap in measurements at approximately 12:00 is due to no τ_2 analysis being performed, although the purification system itself continued to operate.

In a two-phase TPC, the LAr level must be accurately controlled within the extraction region, since any variation of the level within this region can modify the effective extraction field, and may therefore effect the charge extraction efficiency.

ARIADNE has a variety of dedicated sensors to precisely monitor the LAr fill level. An internal cryogenic (Microsoft HD-3000 [3]) webcam provides video footage of the extraction region for easy - albeit qualitative - visual inspection, and a more quantitative approach is to use the capacitance between the extraction grid and the bottom plane of the THGEM. However, due to the large area of the THGEM, this method was found to be extremely sensitive to small fluctuations in the LAr level, which naturally occur during filling, and also to wetting of the THGEM. In addition, neither of these methods provide information about the flatness of the LAr fill level. To remedy this, ARIADNE is equipped with 3 Baumer U500 series ultrasonic distance measuring sensors [23] - as shown in Figure 19, mounted just below the underside of the top flange, which precisely and quantitatively monitor the fill level in three locations.

Calibration of the sensors was performed prior to closing the detector, and involved first confirming (using an external testing setup) that each sensor has the same response over their common operating range. The sensors were then mounted at their respective positions above the

TPC, with fine adjustments to the height ensuring that they all give the same readout value with respect to a common reference point - the TPB-coated glass plane. The sensors were then rotated to their final positions facing over the sides of the TPC, giving an unhindered view of the liquid.

These sensors have been successfully operated to temperatures as low as -40°C, which is considerably below the minimum temperature of the underside of the top flange when the cryostat is filled. The nature of ultrasonic sensors in general means that they are sensitive to changes in pressure and temperature, but relative measurements between the sensors will still be reliable, and so by combining measurements from the sensors, it is possible to both measure the absolute level, and also ensure that the level is uniformly flat across the entire extraction region. The flatness of the fill level relative to the THGEM and extraction grid is adjusted by small adjustments to the six cryostat wheels.

Figure 19: One of the three Baumer Ultrasonic sensors that are used to measure the flatness and fill level of LAr within the ARIADNE cryostat. All three are mounted at the same height - a few centimetres below the underside of the top flange.

Once the LAr filling process is complete, heat losses of the cryostat will cause the LAr to slow boil off, thus increasing the internal pressure and affecting the LAr fill level. To ensure that the LAr remains liquid inside the cryostat, a Cryomech AL300 cryorefrigerator unit [24], installed on the underside of the top flange and shown in Figure 20, is used. When operating at 50Hz and 80K, this provides a peak of 266 W of cooling capacity to the internal volume of the cryostat to overcome the aforementioned heat losses, and so - by adjusting the heat input to the cryorefrigerator's cold head such that the pressure inside the cryostat remains fixed - a stable LAr level is ensured.

2.6 Laser Calibration System

The use of lasers for calibration in LAr detectors has been previously been demonstrated by multiple groups [25], taking advantage of the three photon excitation process that allows the ionisation of argon atoms [26]. In the same vein, the ARIADNE detector features a calibration system that utilises a pulsed Nd:YAG (neodymium-doped yttrium aluminium garnet) UV laser.

Figure 20: The Cryomech AL300 cryorefrigerator cold head extending down from the top flange of ARIADNE. A flexible kapton heater element wrapped around the cold head regulates cooling, and thus allows the pressure in the cryostat to be accurately controlled.

The main purpose of the laser calibration system is to allow measurements of the overall field uniformity to be taken, in both the vertical and horizontal planes. These measurements can then be used to make corrections for any significant non-uniformities in the field during offline analysis and event reconstruction. Non-uniformities can be identified using the principle that - upon entering the active volume - the laser photons ionise the argon atoms, and the free electrons are drifted to the gas phase of the TPC in the same way as ionisation electrons from a particle track would be. Therefore, the resulting EMCCD images will be affected by any non-uniformities in the drift field.

The specific laser used on the ARIADNE detector is a Quantel Q-Smart 100 [27] pulsed Nd:YAG laser, shown in Figure 21 and emitting 1064 nm light at 100 mJ per pulse. Harmonic modules are used to change the wavelength to 266 nm, in the process reducing the pulse energy to 20 mJ. The compact dimensions of the laser allows it to be vertically mounted directly onto the top flange of the cryostat, allowing for a simple and compact design since the beam travels directly into the cryostat through an optical feedthrough, without the need to align the detector to an external optical table.

Suspended from the underside of the top flange is a platform, shown in Figure 22, that holds a UV

Figure 21: The Quantel Q-Smart 100 pulsed Nd:YAG laser, mounted on the top flange of the ARIADNE cryostat, together with the two rotary feedthroughs for controlling the position and orientation of the UV mirror.

mirror at a 45° angle, which acts to redirect the vertical laser beam into the horizontal plane. The entire structure is constructed from VICTREX PEEK 450G - the same material that the TPC support rods are constructed from, to minimise any potential differences between the thermal expansion of the laser support structure and the TPC, so as to reduce vertical misalignments between the relative position of the laser beam and the field cage.

The laser support structure has mechanical elements which allow for manipulation of the position and orientation of the mirror, and hence the horizontal beam. These elements are controlled using two independently-operated rotary feedthroughs on the top flange, as shown in Figure 21. One of the rotary feedthroughs is connected to a lead screw that, when rotated, moves the mirror platform up and down via a lead screw nut rigidly connected to the platform, therefore allowing the beam to be traversed vertically along the entire height of the TPC. Connected to the second rotary feedthrough is a keyed rod which is connected to a corresponding toothed hollow rod on the platform, and rotating this rod adjusts the angle of the mirror - and thus the direction of the laser beam - in the horizontal plane.

The TPC has been designed with gaps in the field-shaping rings, shown in Figure 23, which allow the laser beam to pass into the active volume at specific heights. There are eight small-width gaps, evenly spaced in a vertical line spanning the full height of the TPC, which together permit a vertical scan of the TPC by the laser, and a single wider gap at the bottom of the TPC that allows for a full horizontal scan. Corresponding holes have been cut into the reflector panels on the near side of the TPC.

A COMSOL simulation was performed to investigate the effects of these ring gaps on the TPC drift field, and the results are shown in Figure 24. There is a $\approx 15\%$ non-uniformity of the drift field extending into the TPC for several centimetres, which is similar in magnitude to the non-uniformity induced by the beam plug (as discussed in Section 2.7). As also noted previously in Section 2.1, these non-uniformities subside to an acceptable level within just a few centimetres, but the uniform drift field on that face of the TPC can be restored in the future by replacing the gap-containing rings with standard ones, if these ring gaps are no longer required.

2.7 Cryostat, Top Flange and Beam Plug

Containing all of the previously discussed components of the detector, the ARIADNE cryostat consists of a vacuum-jacketed body and top flange, with mylar super-insulation installed inside the jacket to minimise heat losses. The cryostat is rated for operating pressures of up to 4 bar(g), and has a rated capacity of 1530 litres at 95% full.

A DN200 conflat (CF) flange is welded to the outer wall of the cryostat, and is used to mount the external 0.9 mm thick stainless steel beam window. Correspondingly, the inner wall of the cryostat has a DN160 CF flange axially aligned to the DN200 flange on the outer wall, and the beam plug - which extends into the cryostat - is mounted onto this inner-wall flange.

The cryostat is supported by six height-adjustable wheels. In the case of beamline operation, these wheels allow the beam window and plug to be aligned to the height of the beam.

The top flange, shown in Figure 25, houses the various ports and feedthroughs for mounting the
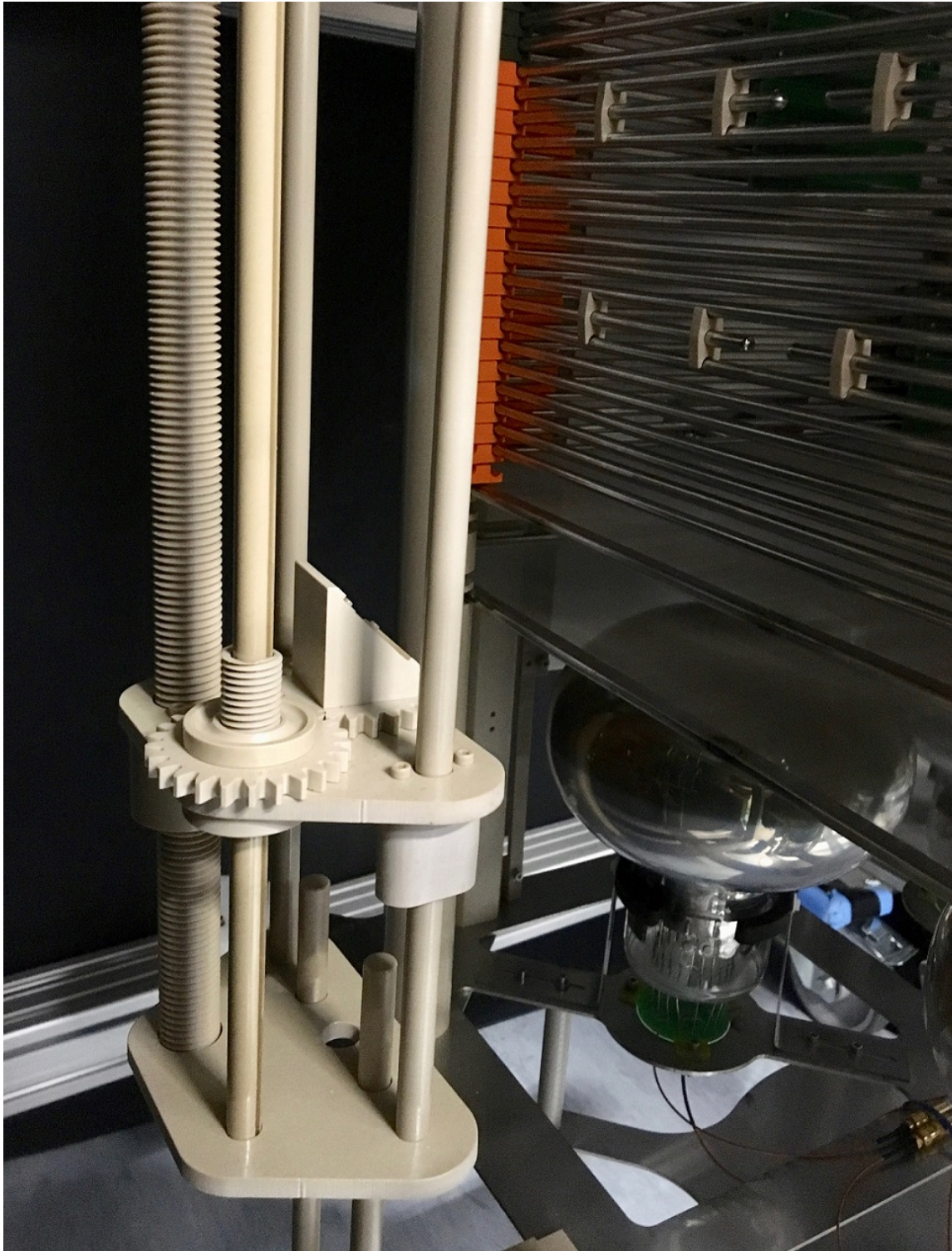
Figure 22: The lower section of the laser support structure, showing the platform with the angled mirror facing towards the TPC. Also visible are the gaps in specific field-shaping rings that allow the laser beam to enter the active volume. For clarity, the reflector panel for this side of the TPC is not shown.

Figure 23: One of the eight small-width gaps in the TPC. The cut ends of the field-shaping ring have been smoothed and polished, to remove any sharp edges that might affect the drift field, and the gap is supported by PEEK elements.
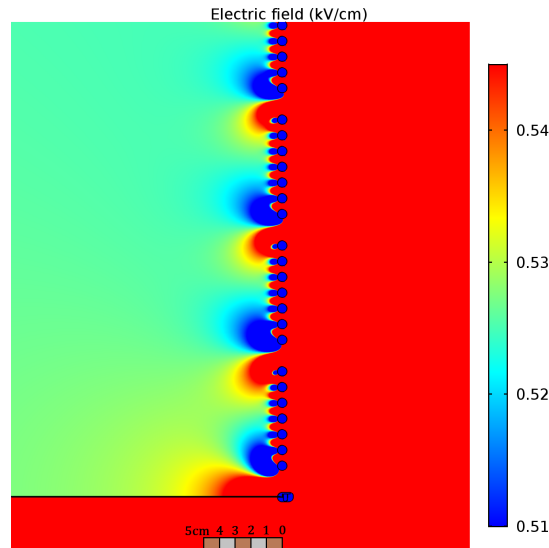

Figure 24: The results of a COMSOL simulation of the effect of the gaps in the field-shaping rings on the drift field. The non-uniformity is ≈ 15% - similar in magnitude to the effect of the beam plug (discussed in Section 2.7) - and extends up to ≈ 3 cm into the TPC, as indicated by the scale bar at the bottom.

external components and providing power, readout and other information to and from the internal components.

Some of these ports have been positioned in specific locations for specific purposes. Of particular note, the EMCCDs (described in more detail in Section 2.8) are mounted on 4 DN200 CF ports with additional DN200-to-100 CF zero-length reducer viewports. These four ports are arranged in a 2 × 2 array centred the vertical axis of the cryostat. The previously discussed cryorefrigerator unit is mounted on a dedicated DN160 CF port, and the aforementioned HV

feedthrough also has a specific location - a DN75 CF port located directly above the cathode grid torus, as does the turbo pump which aids in evacuating the cryostat to ultra-high vacuum prior to introducing LAr. There is also a custom DN63 CF port positioned centrally on the top flange, which could be used for future optical readout R&D. Other ports are populated by the various non-location-specific sensors, viewports and feedthroughs necessary for operating the detector.
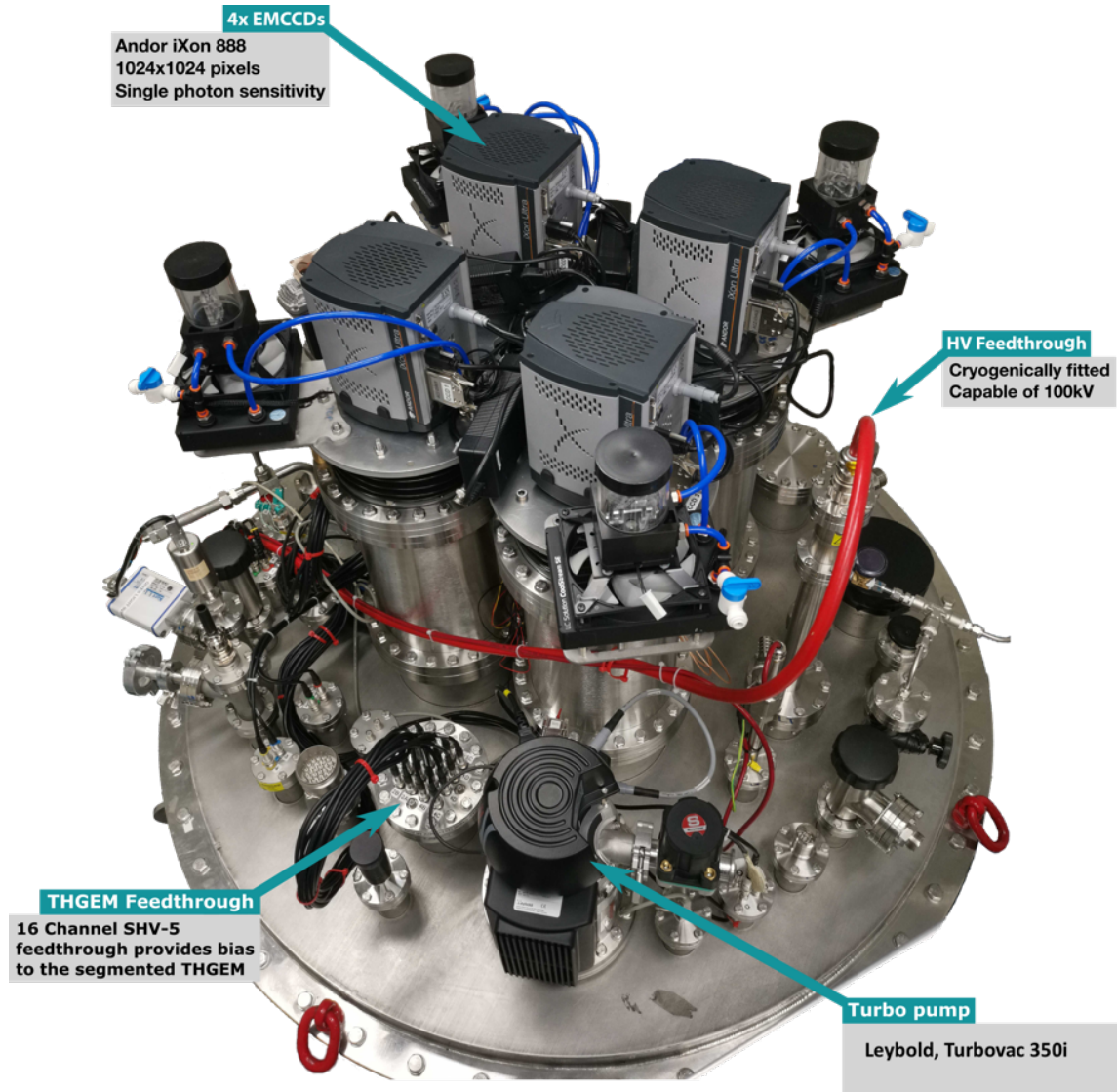

Figure 25: The top flange of the ARIADNE cryostat. The 4 EMCCDs are mounted on the 2×2 array of DN200 CF ports, and various other ports are occupied by feedthroughs for the internal detector components, pressure and temperature sensors, viewports, valves and other external components.

The seal between the top flange and the cryostat body is made using a Viton® Grade "A" gasket, which was chosen for its ability to maintain a flexible and stable seal at a temperatures as low as -20°C [28] - well below that of the underside of the flange even when the cryostat is filled. The

cryostat additionally has a machined groove which would allow the placement of a 2 mm diameter indium seal, if so required.

Without the presence of the beam window and plug penetrating through the cryostat body, incoming particles would encounter a significant amount of material before entering the active volume of the TPC - this scenario is shown in Figure 26a. The overall effect of this material on the quality of the incoming beam can be characterised using the radiation length, X_0 - the distance that a particle can travel through a particular material before its energy is reduced to $1/e$ of its original value. Table 1a shows the thicknesses and corresponding radiation lengths for the materials that an incoming particle would encounter in the scenario of there being no beam window or plug.

    The beam window and plug together form a continuous extension to the cryostat body's vacuum jacket, and so incoming beam particles can travel much deeper into the detector without impedance from any material. This in turn minimises losses and deviations to the incoming particle momenta and direction. The addition of the beam window and plug is shown schematically in Figure 26b, and Table 1b shows the material budget for the scenario of beam transport into the TPC via the beam plug. (The addition of a UHMWPE displacement element is discussed below.) The use of the beam window and plug therefore reduces the energy loss of particles entering the TPC significantly - from 90% to less than 20%.

    Since the beam plug is electrically grounded to the cryostat, its distance from the field cage must be carefully controlled. COMSOL simulations were performed to determine the minimal spacing required between the field cage and the beam plug to avoid LAr breakdown. This has previously been observed for fields as low as 40 kV/cm [29], and so this value was used as the upper limit on the electric field between the beam plug and the field cage. Figure 27 shows the results of the COMSOL simulation with the beam plug installed at ≈ 10.5 mm from the field cage, indicating that the electric field does not exceed the limit of 40 kV/cm.

With the beam plug extending to its minimum safe distance from the field cage, the beam must still be transported through the remaining 19 mm of uninstrumented LAr to reach the active volume of the TPC. Even this thickness would affect the quality of any incoming beam, and so to displace this material, an UHMWPE element is attached to the field cage. This element fills almost the entire space between the end of the beam plug and the active volume, and - since UHMWPE has a much longer radiation length of ≈ 50 cm - helps to maintain the incoming beam quality, while not affecting the shape of the electric field near and around the beam plug.

2.8 EMCCD Cameras

In order to achieve the best possible energy resolution and lowest possible energy threshold, it is important to maximise the collection efficiency of the S2 light produced at the THGEM. To that end, ARIADNE uses four Andor iXon Ultra 888 EMCCD cameras [10] to capture this light - these were previously shown in Figure 25, with additional side-on views shown in Figure 28.

    Each EMCCD is coupled to a Spacecom VF50095M lens (with a speed of f/0.95 and focal length of 50 mm), and all four devices are securely fixed to a common mounting plate positioned above the 4 DN200 nipples on the top flange of the cryostat. This plate has been finely machined to ensure that the EMCCDs are all flat relative to each other, and its tilt can be adjusted to a very
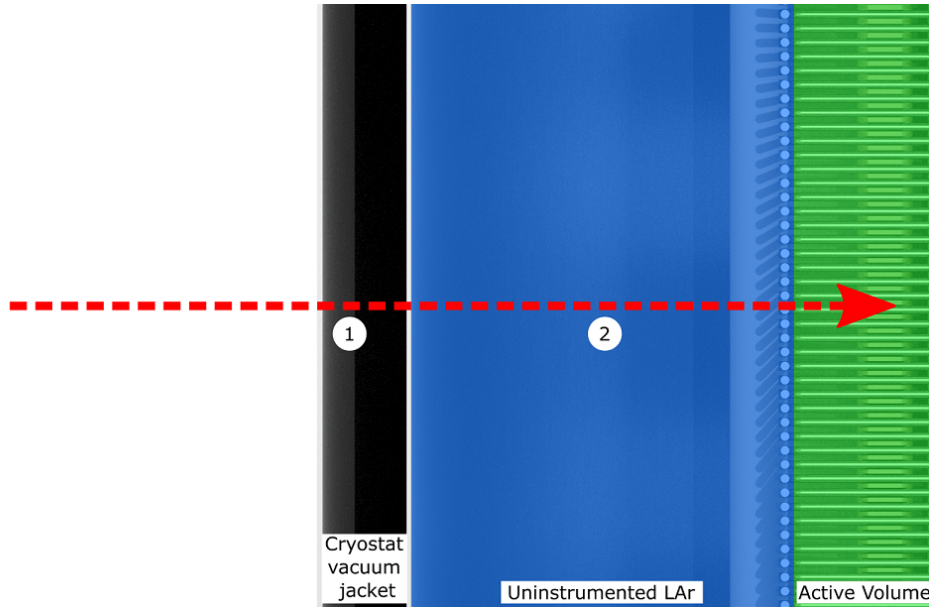
(a) Beam transport through an unmodified ARIADNE cryostat, where the incoming beam passes through both cryostat walls (1) and a large length of uninstrumented LAr (2). In this configuration, the total material budget is 2.29 X_0.
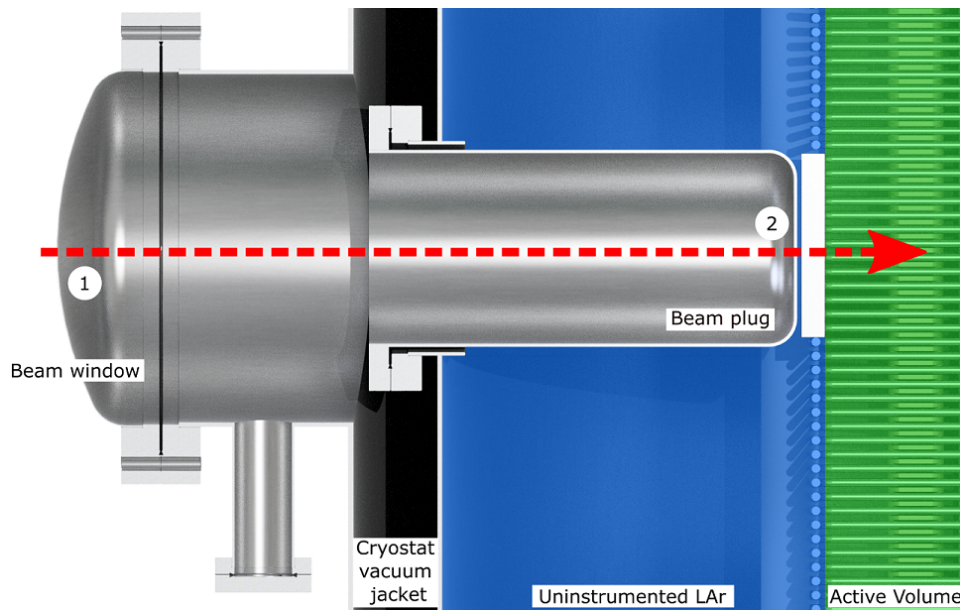
(b) Beam transport through the ARIADNE beam window, plug and UHMWPE element. The incoming beam first passes through a 0.9 mm thick stainless steel beam window (1), and then vacuum until exiting the beam plug through a 2 mm thick stainless steel wall (2). Particles then pass through a 3.5 mm thick slice of uninstrumented LAr followed by a 16 mm UHMWPE element before reaching the active volume. The total material budget for this design is 0.21 X_0.

Figure 26: Scenarios for beam transport from outside the ARIADNE cryostat into the active volume of the TPC.

Material	X_0 (cm)	Thickness (cm)	Thickness (X_0)
Stainless Steel (outer cryostat wall)	1.76	0.4	0.23
Stainless Steel (inner cryostat wall)	1.76	0.3	0.17
LAr (uninstrumented)	14.0	26.4	1.89
Total			**2.29**

(a) The material budget when the beam transport occurs through an unmodified ARIADNE cryostat.

Material	X_0 (cm)	Thickness (cm)	Thickness (X_0)
Stainless Steel (outer beam window face)	1.76	0.09	0.05
Stainless Steel (inner beam window wall)	1.76	0.2	0.11
LAr (uninstrumented)	14.0	0.35	0.02
UHMWPE (displacement element)	50.0	1.6	0.03
Total			**0.21**

(b) The material budget when the beam transport occurs through the ARIADNE beam window and plug.

Table 1: Material budgets for beam transport from outside the ARIADNE cryostat into the active volume of the TPC.
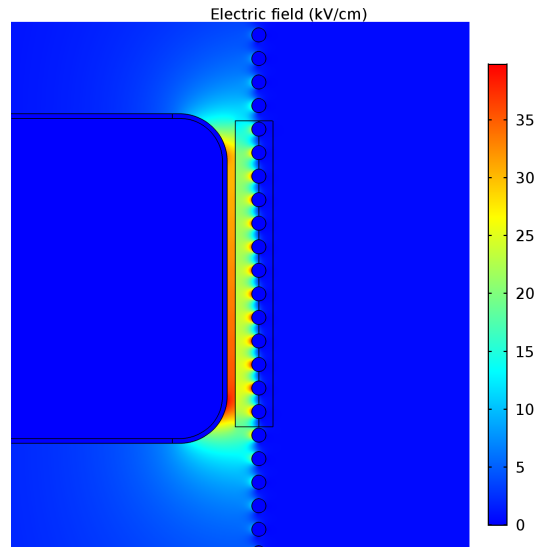

Figure 27: Results of a COMSOL simulation of the electric field in the region outside the field cage near the end of the beam plug. The length of the beam plug was carefully chosen to ensure that the field between the beam plug and the field cage does not exceed 40 kV/cm - a safe lower limit for the dielectric strength of LAr. The UHMWPE element, discussed in the main text, is also shown.

fine level using threaded rods, allowing for precise alignment of the EMCCDs' flatness relative to the THGEM inside the cryostat. This has been achieved by matching the plate's tilt to that of the THGEM, which has been measured to the order of 0.1° using a high-precision level finder. The lenses and top of each DN200 nipple are fully enclosed by rubber bellows, which ensure light tightness while still allowing access to the lenses' focus and iris controls when required. The external location of the mounting assembly also gives excellent access to the EMCCDs, allowing them to easily be maintained and upgraded.
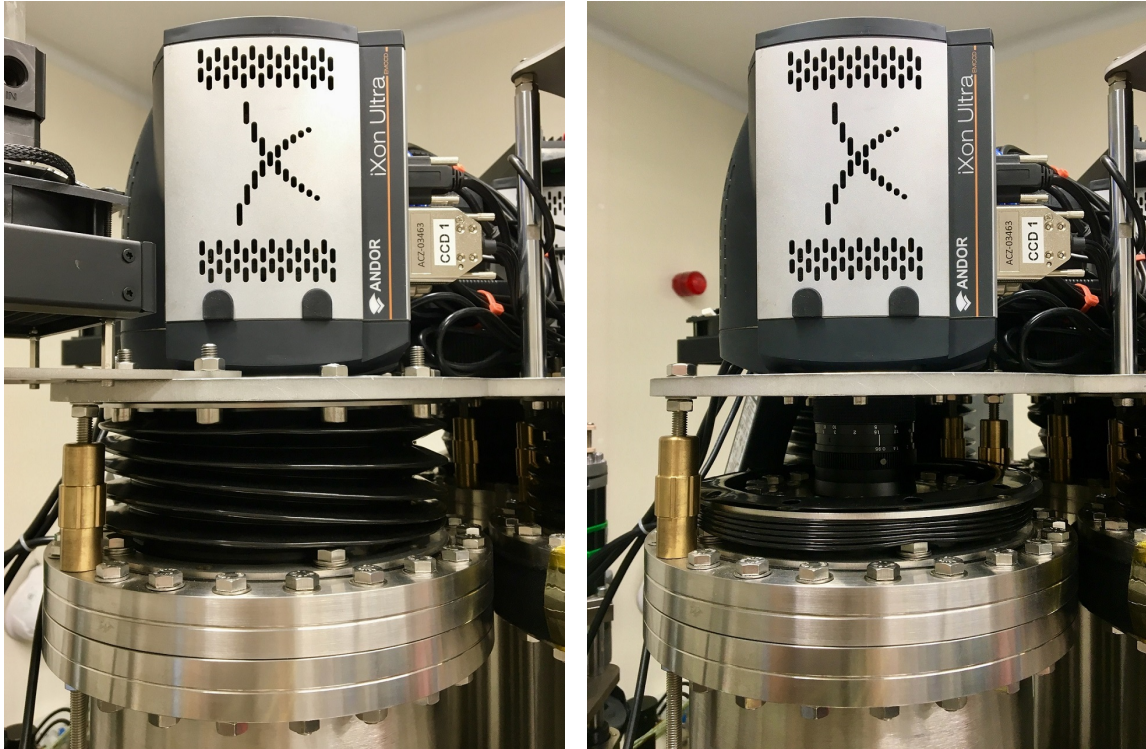
(a) With the rubber bellow secured in the "up" position, ensuring light tightness.

(b) With the rubber bellow in the "down" position, allowing access to the Spacecom lens.

Figure 28: Side views of one of the Andor EMCCDs in position on the common mounting plate, which is in turn secured to the 4 DN200 nipples on the top flange of the ARIADNE cryostat.

The sensor used in each of the EMCCD cameras has a quantum efficiency of approximately 80% at 420 nm (the peak wavelength of the TPB emission spectrum), as previously shown in Figure 13, and the cameras as a whole are single photon sensitive. This is achieved through the use of EM gain - applied on a linear multiplicative scale up to a maximum factor of 1000 - to amplify the incoming photon signal above the readout noise of the charge amplifier. They have a full well depth of up to 80,000 e^-, which is sampled at 16-bit digitisation, giving relative intensity measurements of up to 65,356 ADU per pixel, and so allowing high resolution calorimetry.

During readout, the pixels can optionally be grouped into square clusters of 2×2, 4×4, 8×8 or 16×16 pixels per cluster - this is referred to as the "binning". A readout rate of approximately 60Hz can be achieved when running the cameras in 4×4 binning - this setting was found to give a

good balance between track resolution and collected light per binned pixel. Each camera's binning settings are easily changed, which allows for quick detector reconfiguration and switching between high resolution tracking of high intensity signals or coarse resolution tracking of faint light signals using 8×8 or even 16×16 binning.

3 Detector Operation

3.1 Data Acquisition

The ARIADNE Data Acquisition (DAQ) systems govern the synchronised collection of data from the various detector readouts, in a way that is straightforward for both experienced and untrained individuals to use, and allowing for small changes to be made to the acquisition settings as needed during detector operation.

The device readouts are as follows:

- EMCCDs: these have built-in readout and digitisation electronics, and data is transferred over high-speed USB 3.0. Each EMCCD also can output a veto signal, which is active during the process of acquiring a frame (i.e. the time during which the device is not yet ready to start a new acquisition).

- PMTs: the signal from each one is read out by a CAEN V1720 (12 bit, 250 MS/s) digitiser, which has 8 independent channels, each with a time resolution of 4 ns per sample.

- THGEM: the signal from each of the 16 pads is split by a pre-amp into high- and low-gain channels, giving a total of 32 charge readouts. These are read out by a 64-channel CAEN V1740 (12 bit, 62.5 MS/s) digitiser, with a per-sample time resolution of 16 ns.

Due to the maximum event rate being limited to approximately 60Hz (constrained by the EMCCD readout rate previously discussed in Section 2.8), the technical requirements for full detector DAQ are not demanding, and the relatively low event rate means that all incoming data can be stored directly to disk, without the need for any online filtering of events.

The central point for the DAQ is a dedicated desktop computer - the "DAQ PC", which handles all parts of the DAQ (control, operation, settings and data storage), as well as slow control and monitoring (discussed in Section 3.3 below).

Figure 29 shows an example of the DAQ Graphical User Interface (GUI). This software package - written specifically for ARIADNE by the authors, and run from the DAQ PC - allows control of the DAQ system, including selection of the particular devices being used, configuration settings for each device, and parameters particular to the run such as the number of events to record and what trigger mode to use.

Alongside the GUI, an Event Viewer - shown in Figure 30 - has been developed which can be operated in either "Live" (showing data as it is processed during a run) or "Offline" (showing data previously saved to disk) mode. As well as making use of GPU acceleration to produced high quality output of PMT and THGEM data, there are several basic tools built into the Viewer - for example, manipulation of level thresholds in the EMCCD event display, and automatic basic statistical calculations (mean, maximum, etc.) on the data. The Viewer can therefore be used at all stages of detector operation - during commissioning, for data quality checks during data-taking, and for basic visual analysis after data-taking is complete.
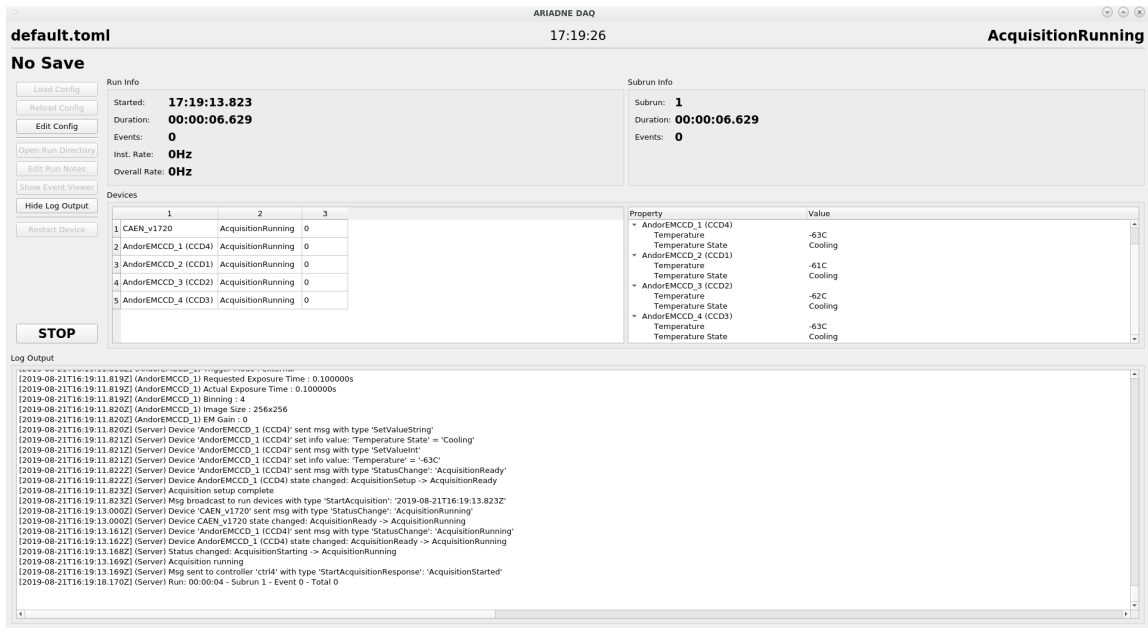
Figure 29: The DAQ GUI, operating in "No Save" mode (used for debugging and small optimisations, where saving the data is not required). A list of available devices and their current parameters is seen at centre, and current run and subrun information is shown across the top. The window at the bottom is for general logging output.
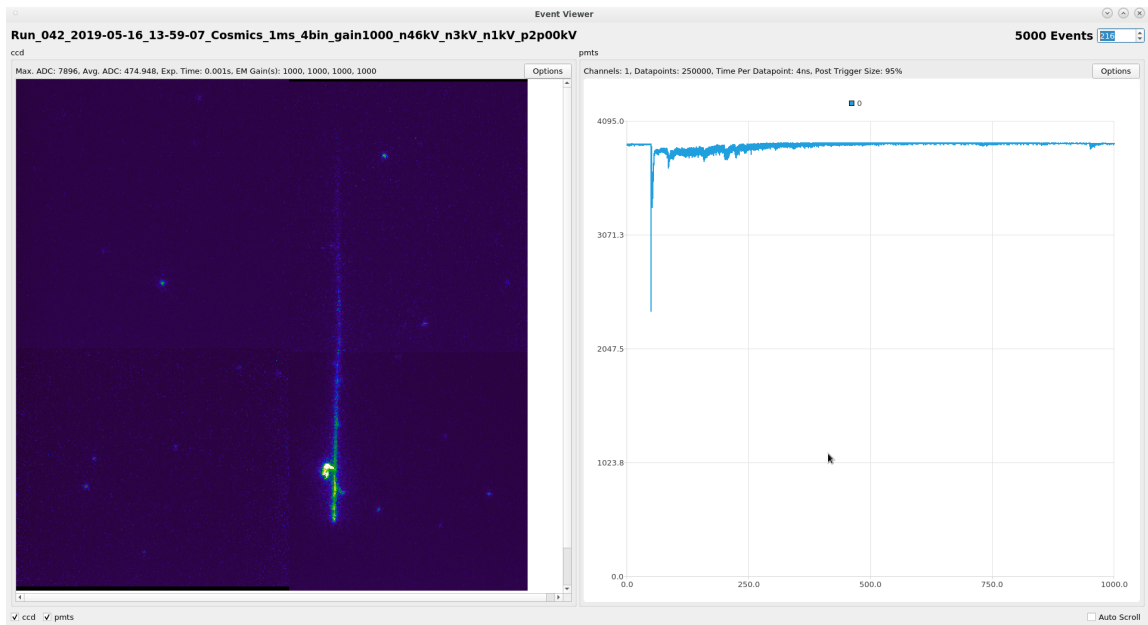

Figure 30: The Event Viewer operating in "Offline" mode, showing the EMCCD and PMT outputs for a single cosmic muon event. (Only one PMT signal is shown here for clarity.) The acquisition settings for each device are displayed above the respective output.

3.2 Trigger System

Figure 31 gives a schematic overview of the global ARIADNE detector trigger system. (Note that this only covers the implementation for the detector itself - additional external trigger sources were used during operation at the CERN T9 Testbeam, but they are discussed in Chapter 4.3.)

The trigger system is implemented in NIM logic. Each of the PMTs issues a "local" (i.e. device-level) trigger via the V1720 digitiser, and these are all passed to a "trigger distribution" FPGA, which identifies an internal combined PMT trigger for the entire detector if it finds that any one of the individual PMT triggers is above a pre-defined threshold.

If the combined PMT trigger is found to be in coincidence with a veto signal from any of the EMCCDs, no further triggers are issued, and the device readouts are reset. If no veto signal is present, i.e. all four EMCCDs are ready to read out, a "global" trigger is issued by the FPGA and distributed to the PMT and THGEM digitisers and the EMCCDs, signalling them all to begin data readout.

3.3 Detector Monitoring and Slow Control

The detector has a number of real-time monitoring and slow control systems.

Internally-positioned thermocouple temperature sensors, placed at the bottom, middle and top of the field cage, are used to measure the temperature within the cryostat, and so also provide information about the LAr level during filling, operation and emptying of the detector. A fourth internal thermocouple is used to monitor the temperature of the underside of the top flange, and the external temperature of the cryostat - and therefore the performance of the vacuum jacket - is monitored using a further two thermocouple sensors, mounted on the outside of the cryostat body and the outer surface of the top flange.

As previously noted in Section 2.5, the LAr level can also be monitored via a set of ultrasonic sensors as well as a webcam, positioned such that it has a view of the gap between the THGEM and extraction grid, as seen in Figure 32. A second webcam provides a view of the top of the internal filtration cartridge, which allows for the performance of the recirculation system to be monitored. Externally-controlled LEDs are positioned around the top of the TPC to provide illumination for the webcams.

Finally, three pressure sensors - a Kurt Lesker Series 910 covering the range from 1×10^{-5} to 2000 mbar, an Agilent PCG-750 for the range between 5×10^{-5} and 1500 mbar, and finally a Kurt Lesker HPT-100 operating from 1×10^{-9} to 1000 mbar - are available to monitor the internal cryostat pressure. The normal operating pressure of the detector is no more than 1.2 bar and so the Kurt Lesker 910 and Agilent sensors allow monitoring even in an over-pressure situation.

The data from all of the monitoring devices is passed to a Grafana server running on the DAQ PC, which provides a centralised way to monitor the immediate values, as well as longer-term trends. This server can be accessed locally (i.e. on the DAQ PC itself), or remotely from any internet-connected browser using the correct user credentials. An example of the monitoring display on the DAQ PC is shown in Figure 33.
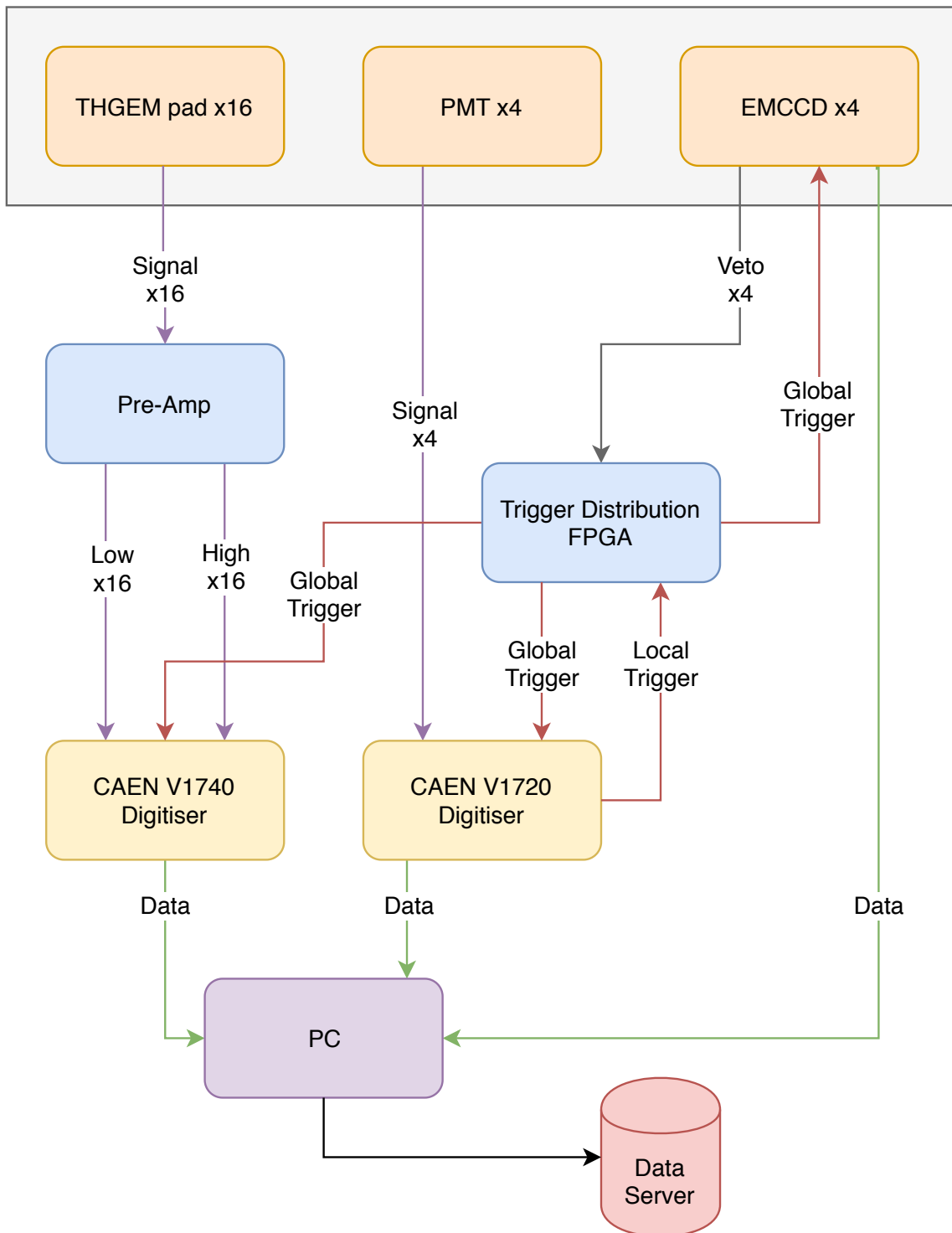
Figure 31: Schematic of the ARIADNE trigger and readout system, as implemented only for the detector itself.
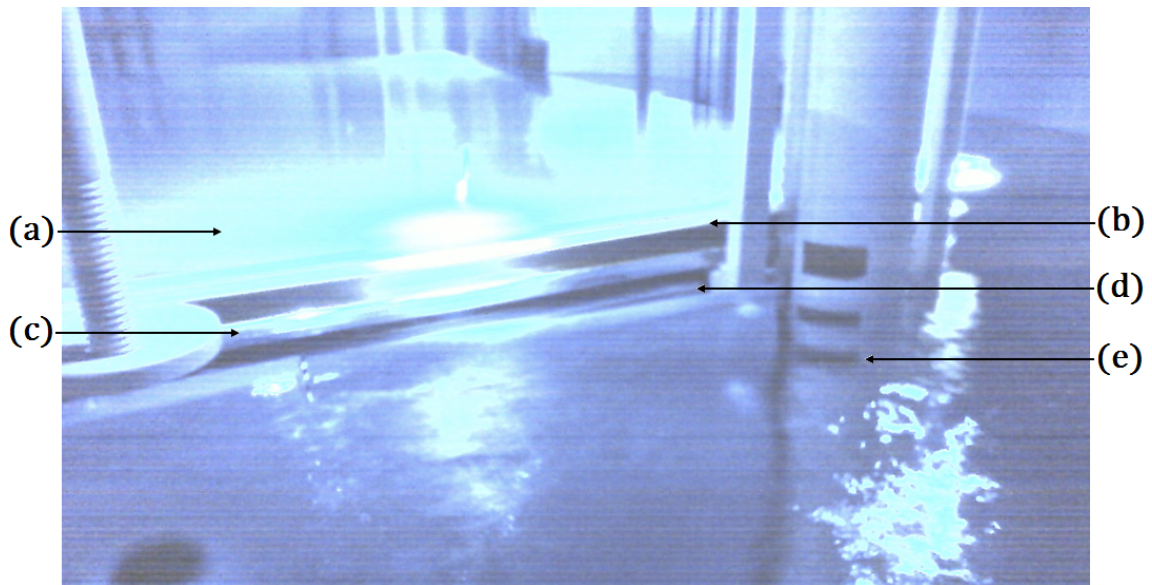
Figure 32: An internal view of the cryostat, taken using one of the cryogenic webcams while the detector was being filled. The TPB-coated glass (a), THGEM (b), extraction grid (c) and first field ring (d) can be seen, with the LAr level just below the ring. The markings on the PEEK support rod (e) are used to help determine the LAr level.
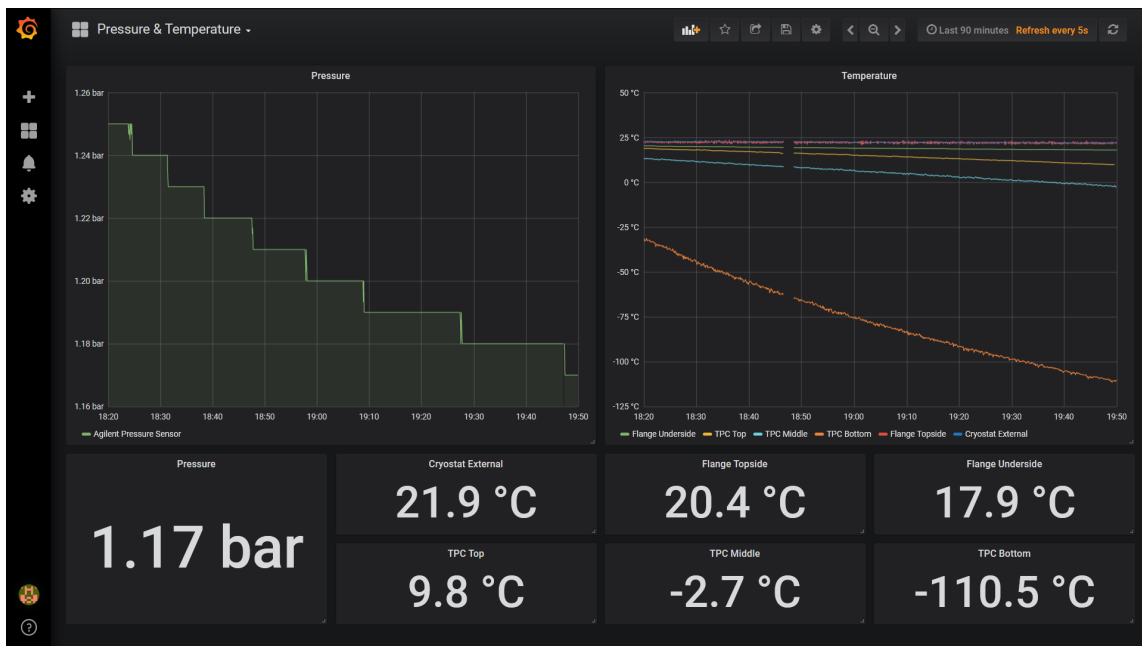

Figure 33: The Grafana monitoring display, showing the pressure and temperature sensor readouts. The numerical values are the immediate values, and the graphs allow longer-term trends to be observed. When this image was taken, the detector was being filled with LAr.

The monitoring system is linked to an automated alert system, which is capable of automatically sending messages to the ARIADNE collaboration's internal messaging service in the event of any temperature or pressure readings crossing preset alert-triggering thresholds. This provides a level of protection in the case of problems such as a cooling system failure or power outage, and gives detector operators time to physically access the detector and resolve any issues.

3.4 Nearline Analysis - Image Stitching

When the EMCCDs are correctly focused to the plane of the THGEM, the field of view (FoV) of each EMCCD is larger than one quarter of the THGEM's area.

This results in some overlap between adjacent EMCCDs' FoVs, as well as a view of the region outside the THGEM's outer edges. To correct for these overlapping FoVs, a simple "image stitching" algorithm is applied to the raw EMCCD data. This involves cropping each individual image according to empirically calculated margins, followed by translating the images to remove the now-empty space between them. The process is shown schematically in Figure 34. Since the EMCCD positions and FoVs do not change over the detector's operational lifetime, the same stitching algorithm is applicable to all raw EMCCD data, and in the discussions of results in Sections 4.4 and 5.3 below, image stitching is always implicitly performed.

Using the 4×4 binning scenario as an example, the dimensions of each single EMCCD image after stitching is approximately 480×480 pixels. Given that this corresponds to the physical 53×53 cm area of the THGEM, the spatial resolution at this binning is therefore ≈ 1.1 mm per pixel. Similar calculations show that the resolution is 2.2 and 4.4 mm per pixel for 8×8 and 16×16 binning respectively.
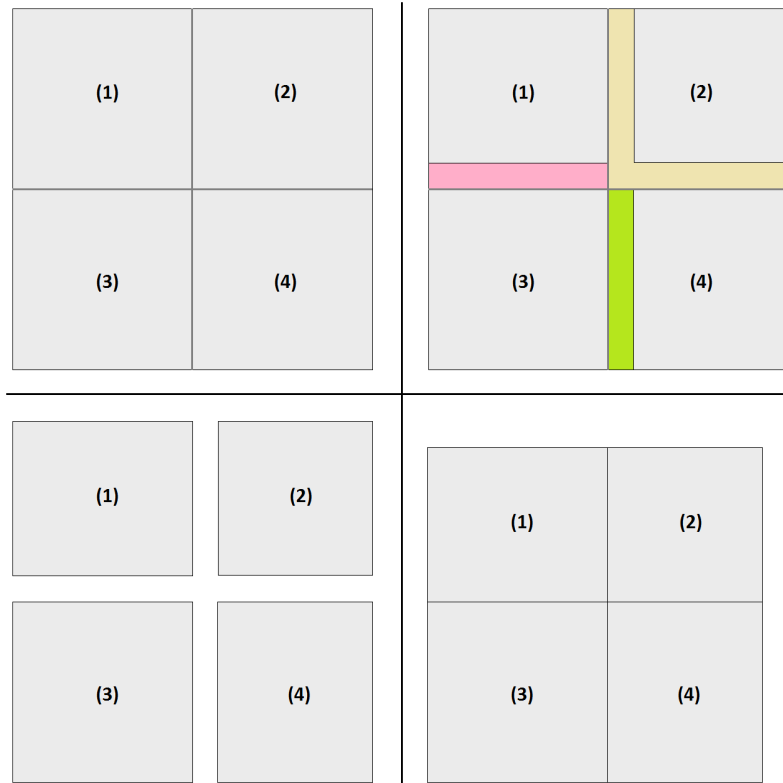
Figure 34: The image stitching process for producing a single EMCCD image per event. The raw image (top-left) is square, as is each EMCCD's individual FoV. The overlaps between adjacent FoVs are first identified (top-right), depicted in pink, yellow and green for EMCCDs 1, 2 and 4 respectively, and then removed (bottom-left), leaving the EMCCDs with non-square, but now unique, FoVs. The sizes of these overlaps have been found empirically across a large number of raw images. The final step is to translate the FoVs such that they align to the same outer edges, resulting in an overall square image - slightly smaller than the original raw image - containing no overlaps or empty space (bottom-right).

4 Mixed Particle Detection at the CERN T9 Testbeam

4.1 T9 Testbeam

In order to characterise the response of the ARIADNE detector and its various sub-systems, a well-described source of particles spanning a range of energies is required. The T9 testbeam at CERN [30] was chosen for this task. The T9 beam line, located in the East Hall of the CERN Meyrin site, is initiated by a proton beam from the Proton Synchrotron (PS) striking a stationary aluminium or beryllium target. This produces a mixed beam of electrons, muons, pions, kaons and protons (along with their respective anti-particles) at momenta ranging between 0.5 and 15 GeV/c. The T9 source is located 55 m from the experimental area, and the beam line is pre-equipped with two in-line Gas Čerenkov counters, as well as an air gap located approximately 20 m from the experimental area, allowing for the placement and use of a Time Of Flight (ToF) system for independent particle identification (PID). A schematic of the T9 beam line is shown in Figure 35.
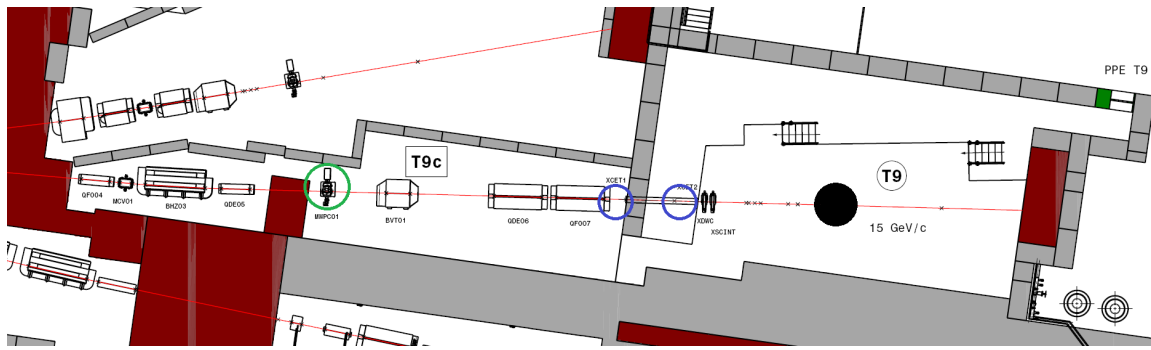

Figure 35: Schematic of the T9 beam line and experimental area within the East Hall (adapted from [30]), with the air gap indicated by the green circle, the two in-line Čerenkov counters by blue circles, and the approximate size and position of the ARIADNE detector by the filled black circle. This view excludes the highly irradiated area closer to the target (to the left of the image), and includes parts of the adjacent T8 and T10 beam lines (below and above T9 respectively).

The ARIADNE detector was operated at the T9 testbeam for 18 days during March and April of 2018, collecting data on electrons, muons, pions and protons (as well as their anti-particles) at momenta between 0.5 and 8.0 GeV/c (the range suggested by the energy containment studies discussed previously in Section 2.1). No kaons were collected, as their short lifetimes mean that the vast majority of them will decay within the beam line before reaching the detector. A total of just under 800,000 events were collected during this period, split evenly between the positive and negative polarities. (Information concerning the relative fractions of each particle species, as measured at the T9 source, can be found in [30].)

4.2 Beamline Hardware

Collimators

The beamline is equipped with a set of collimators, which are used to limit the physical size of the beam, and therefore control the number of particles per spill that reach the experimental area.

The collimators act as 'shutters', with their left, right, top and bottom positions all independently controllable.

Čerenkov Counters

The T9 beamline is also pre-equipped with two in-line Čerenkov counters. Each counter consists of a volume of gas connected to a PMT through an optical viewport. Any particle passing through the counter will emit Čerenkov radiation if it exceeds the phase velocity of light in the gas, the value of which is dependent on the type of gas and its pressure. Therefore, by changing these two properties of the counter, it is possible to use it to tag different particle species travelling at different velocities, i.e. momenta.

When running the ARIADNE detector at T9, one of the Čerenkov counters was filled with carbon dioxide at 2.2 bar while the other one was emptied to vacuum - so as to minimise its impact on the beam as it passed through (the counter cannot be physically removed from the beamline). Only electrons, with their low rest mass, have a high enough velocity at momenta below 8 GeV/c to emit Čerenkov light in 2.2 bar CO_2, and so this Čerenkov counter was used as an electron tagger.

Time Of Flight (ToF) System

For non-electron (muon, pion and proton) PID, a ToF system was designed and built at the University of Liverpool. The system is made of two identical assemblies, each consisting of a $0.15 \times 150 \times 150$ mm EJ-212 plastic scintillator film (manufactured by Eljen Technology) covered by 3M ESR Vikuiti reflector material (the same that surrounds the ARIADNE TPC) to optimise light collection. Each scintillator film is coupled via a fishtail light-guide (also from Eljen Technology) to a 2-inch Hamamatsu H6533 PMT. The EJ-212 scintillator was chosen due to it being specifically formulated for thin films - a desirable attribute for use in-beam, as the particles will lose less energy and scatter less when passing through a thin film compared to a thick one. Each scintillator and PMT assembly is housed within a light-tight 3D-printed frame, which is held at beam height using a frame built from extruded aluminium profile. The ToF assemblies are shown in Figure 36.

As indicated by its name, the key measurement for PID using the ToF system is the time taken for a particle to travel between the assemblies - this time of flight is dependent on both the particle mass and momentum. Since the momenta of the particles at T9 is known (to within 1%), the measured flight time at any single momentum is then solely dependent on the particle mass, and therefore its type.

The two ToF assemblies were read out using a 2-channel, 0.25 ns per sample CAEN V1761 (10 bit, 4 GS/s) digitiser. This is sufficient resolution to distinguish between protons and other particle types at all momenta, and between muons and pions below 0.7 GeV/c. Separating muons and pions above 0.7 GeV/c is not possible with this digitiser, due to the difference between their ToF values being less than the 0.25 ns resolution. The same issue prevents the separation of electrons and muons at momenta above 0.8 GeV/c, hence the usefulness of a separate electron-tagging system by way of the aforementioned Čerenkov counter.

In summary, a reasonable level of independent PID capability can be achieved by combining measurements from both the Čerenkov counter and the ToF system. If a particle is detected by the

Figure 36: The far (left) and near (right) Time of Flight assemblies. The far assembly was positioned in the beamline air gap, and the near assembly directly in front of the detector's beam window. The separation between the assemblies was 18.05 m.

Čerenkov counter and both of the ToF assemblies, it must be an electron. If a particle is detected by both ToF assemblies, but not by the Čerenkov counter (i.e. there is no signal from the counter at the time the particle was expected to pass through it), it must be either a muon, pion or proton. The exact time difference between the assembly signals indicates which of these particles is present, but muons and pions cannot be distinguished above 0.7 GeV/c due to the difference in their flight times being smaller than the digitiser's resolution.

4.3 Operational Configuration

As noted above, operation of ARIADNE at T9 consisted of 18 days of beam running, during which time approximately 800,000 events were recorded over a range of momenta.

To reduce the possibility of pileup between beam particles - that is, two or more beam particles entering the detector within the same event window - the collimators were set so as to keep the

number of particles per spill at approximately 20. The exact collimator positions were determined empirically, with the general trend being that the collimators were more open - and the beam wider - when operating at lower momenta. In all cases, the collimator positions varied between 0.4 and 9.0 mm (where 0mm indicates that that collimator is 'closed').

The ARIADNE detector itself was set up and operated as described above, with the segmented THGEM (previously discussed in Section 2.3) being used for the S2 light production and charge readout. However, the additional beamline hardware described above introduced some extra requirements into the DAQ and trigger system previously described in Section 3.2 and shown in Figure 31:

- The Čerenkov counter was read out using the CAEN V1720 digitiser, in addition to the existing PMT readout on the same device.

- Along the existing requirement of at least one above-threshold PMT signal and no EMCCD vetos, two additional signals were required for a global trigger to be issued: an above-threshold signal from the near ToF assembly (via the CAEN V1761 digitiser), and the presence of the beam-spill signal (provided by T9's own monitoring hardware, and identifying that a spill has occurred). In other words, a particle would only trigger the detector if it was part of a spill and had passed through both the near ToF assembly and the main detector.

- A successfully issued global trigger signal was split between the now 3 digitisers as well as the EMCCDs.

Table 2 shows the various parameters that were used during beam operation, arranged by device.

4.4 Results and Discussion

Figures 37 and 38 present a selection of negative polarity beamline events as captured by the ARIADNE detector. These images represent the first time that argon interactions from a beamline have been optically imaged in a two-phase LArTPC.

The ARIADNE detector was operated at a THGEM field of 27 kV/cm, which is below nominal, due to a manufacturing defect on one of the channels on the 16-channel THGEM feedthrough. Figure 42 (which uses the monolithic THGEM at a lower pressure of 1080 mbar, but is still representative of the segmented THGEM due to similar design and construction) indicates that the electron-multiplying regime becomes prominent at a THGEM field above ≈ 28.5 kV/cm, meaning that CERN testbeam operation was conducted in the low bias regime, resulting in little to no charge gain and considerably reduced production of S2 electroluminescence light. However, even with these limitations, the EMCCD cameras were still able to reliably capture S2 light from argon interactions: the mean background pixel intensity at the EMCCD operating settings given in Table 2 was found to be ≈ 500 ADU, whereas typical pixel intensities along the tracks are seen to be well above this level.

Operation of the ARIADNE detector at the T9 beamline has demonstrated the optical readout

| Parameter	Value	Comments
EMCCDs		
Gain	1000	Maximum available value
Cooling	Water	Allows operating temperature of -80°C, reducing the mean background pixel intensity to ≈ 500 ADU
Binning	4 x 4	Gives a raw image size of 256 x 256 pixels per camera
Exposure Time	400 μs	
PMTs		
Biases	975V 1000V 1175V 850V	Different voltages used so as to equalise the individual PMT responses
Recording Length	100,000 datapoints	Gives an event window of 400 μs, consistent with EMCCDs
ToFs		
Biases	-2250V -2250V	
Recording Length	20,000 datapoints	Gives an event window of 5 μs, beginning at the same time as the global trigger is issued
Field Cage Biases		
Cathode Extraction Grid	-80.2 kV -3.5 kV	Nominal drift field of 960 V/cm
THGEM Top THGEM Bottom	+1.4 kV -1.3 kV	THGEM field of 27 kV/cm
Other		
Cryostat pressure	1.2 bar	

Table 2: Operational parameters for the ARIADNE detector at the T9 testbeam.

method's capability for high spatial resolution: as previously noted in Section 3.4, the resolution of the images at 4×4 binning is 1.1 mm/pixel, which results in extremely well-defined and clear particle tracks.

This EMCCD image resolution is a contribution to the overall detector spatial resolution - others include uncertainties originating in the detector hardware and subsequent analysis methods. Another specific contribution is from electron diffusion within the LAr, which can be split into transverse (in the $x - y$ plane) and longitudinal (in the drift - and therefore z - direction) components, the former of which is directly comparable to the EMCCD image resolution. The amount of diffusion depends on the exact operating parameters of the TPC, with studies [31, 32] indicating that, over a drift length of 80 cm and at drift fields between 0.5 and 1.0 kV/cm, the transverse electron diffusion is ≈ 1 mm - comparable to the EMCCD image resolution. This diffusion increases to ≈ 4.2 mm for a 12 m drift length at the same field (such as the TPC proposed for use in DUNE [33]), indicating that in future large colossal-scale LArTPCs, the overall spatial resolution would not be
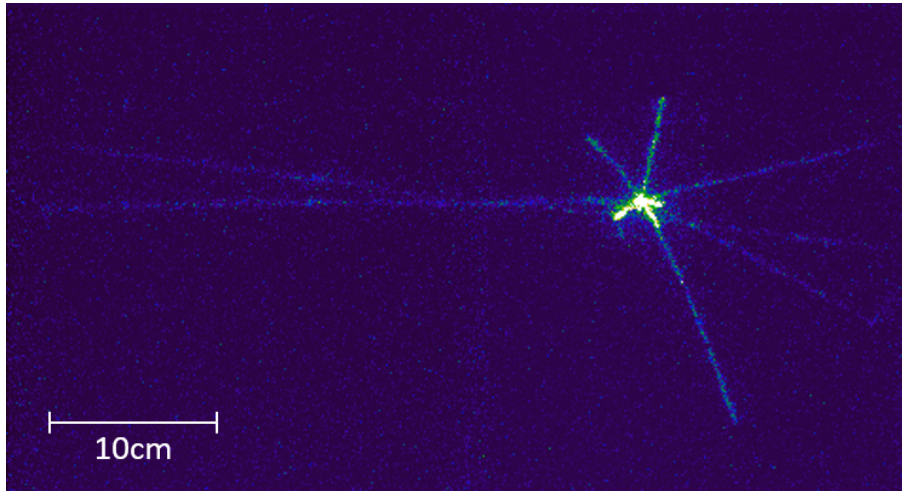
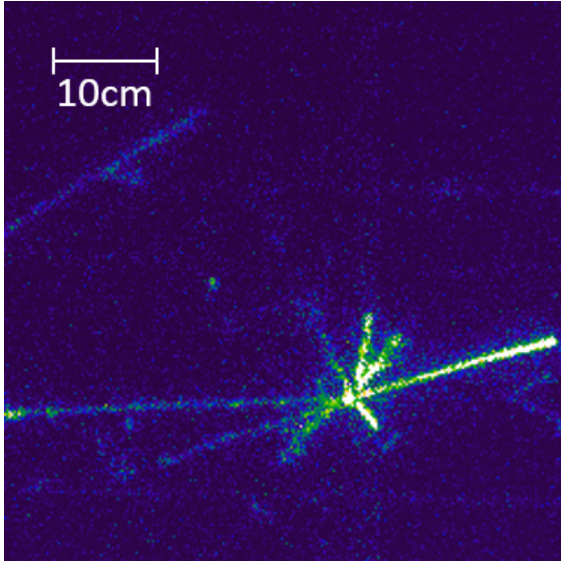(a) 3.0 GeV/c anti-proton candidate, maximum intensity = 21894 ADU
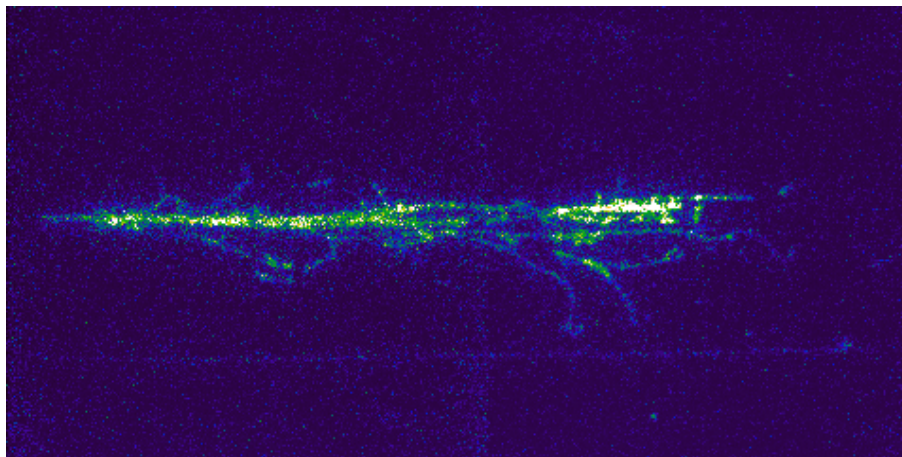
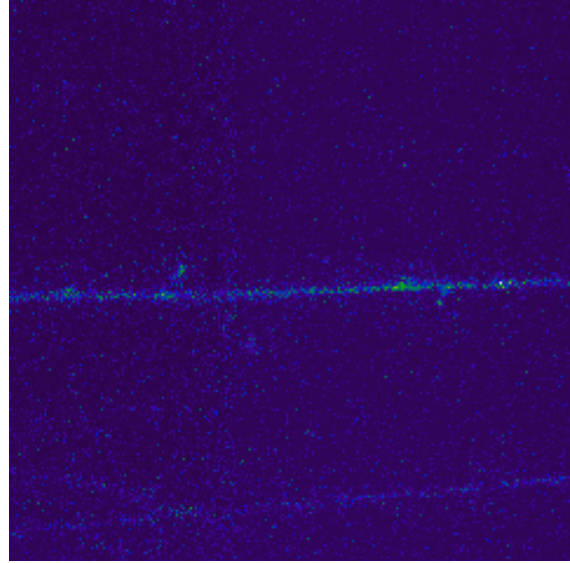(b) 5.0 GeV/c electromagnetic shower, maximum intensity = 12916 ADU
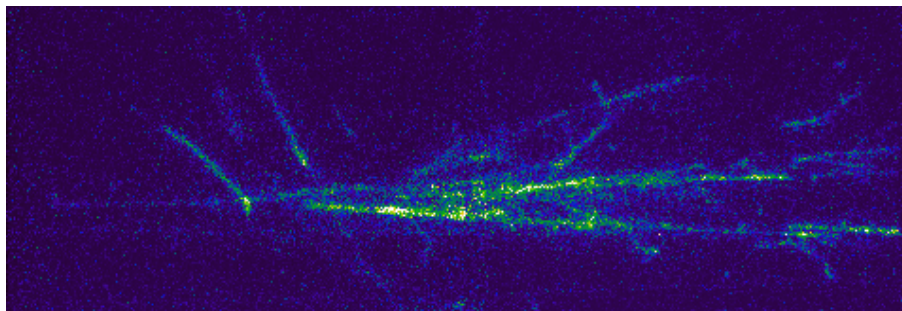
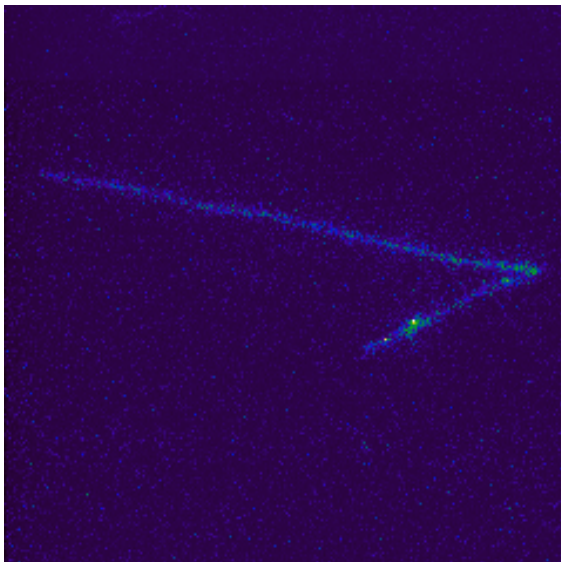(c) 7.0 GeV/c electromagnetic shower, maximum intensity = 7367 ADU

Figure 37: A selection of negative polarity beamline events as captured by the ARIADNE detector. The indicated scale is common to all images.
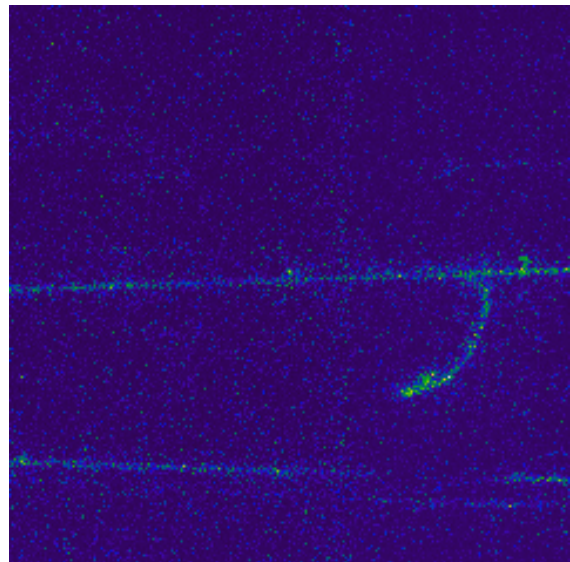
(a) 3.0 GeV/c anti-proton candidate, maximum
intensity = 19372 ADU

(b) 3.0 GeV/c muon candidate, maximum intensity =
4181 ADU

(c) 0.7 GeV/c nuclear recoil, maximum intensity =
5632 ADU

(d) 0.5 GeV/c delta ray candidate, maximum
intensity = 3695 ADU

Figure 38: A selection of negative polarity beamline events as captured by the ARIADNE detector. The indicated scale is common to all images.

dominated by the resolution of EMCCD images at 4×4 binning, but instead by other effects such as the electron diffusion in LAr.

Although the 2D optical readout alone has shown excellent results, full 3D reconstruction of particle tracks requires the combination of EMCCD data with a faster readout channel, such as the

PMT, for z information. In the case of the PMT signal, the absolute z position of a track in the TPC is determined by measuring the time difference between the S1 and S2 pulses, and relative track information, such as the angle of the track, may be determined from analysis of the S2 pulse shape.

Such a method of 3D track reconstruction has already been successfully demonstrated [4], but it requires events with low pileup - that is, a single track on the optical readout corresponding to a single (S1, S2) pulse pair on the PMT signal. If an event contains multiple tracks and/or pulse pairs, it becomes challenging to determine which pulse pair is associated with which track. In the case of the T9 beamline, the majority of events contained a large population of "halo" muons in the 400 μs event window - these are generated during the interaction of the PS proton beam and the East Hall interaction target, and travel in an increasingly wide conical spread towards and through the various experimental areas and detectors therein. These muons - some typical examples of which are shown in Figure 39 - therefore act as a background in many events recorded by ARIADNE at the CERN T9 testbeam.
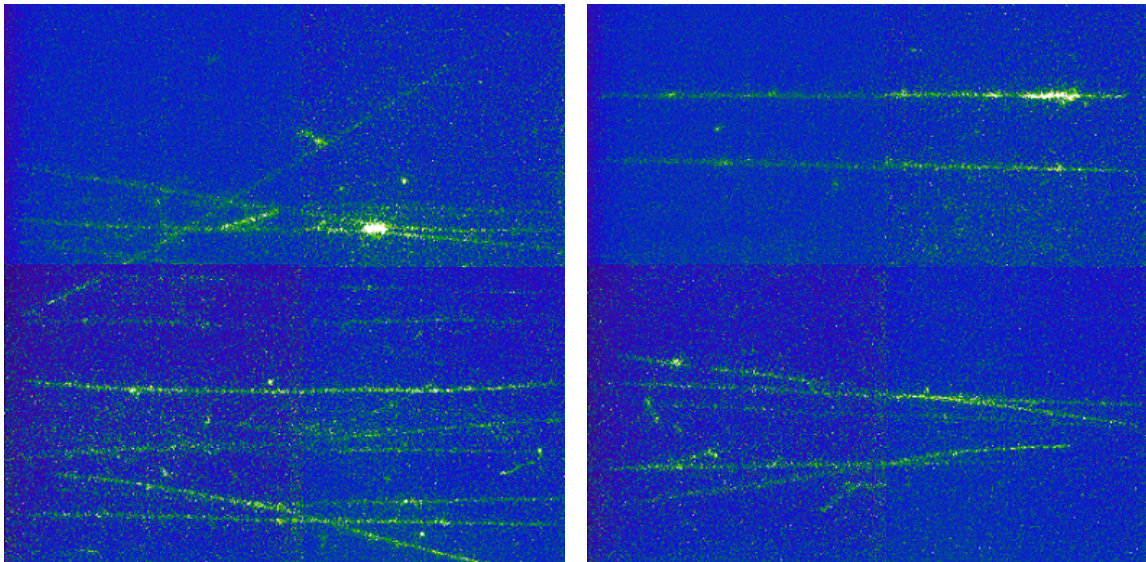

Figure 39: Examples of the "halo" muon background over an event window of 400 μs, generated by the PS / target interaction in the East Hall.

5 Cosmic Muons at the Liverpool LAr Facility

5.1 Cosmic Muons

A number of upgrades, most notably the change to the monolithic THGEM and the installation of the laser calibration system, were performed on the ARIADNE detector following CERN T9 testbeam operation. The detector as a whole has then been calibrated and characterised using cosmic muons.

The expected rate of cosmic muons incident on the 53×53 cm THGEM area is ≈ 50 Hz (based on the known rate of muons at the Earth's surface [34]), and this was indeed observed. This rate is significantly lower than the total rate of incident particles encountered at the CERN T9 testbeam. Pileup is therefore much less of an issue when operating with cosmic muons, allowing for easier correlation between single tracks on the EMCCD images and single (S1, S2) pulse pairs in the PMT signal, and thus full 3D particle track reconstruction, as discussed previously in Section 4.4. A lower pileup rate also means that a longer event window can be used.

Cosmic muons also exhibit a much wider range of geometries and track lengths as they pass through the detector than beamline particles - for example, a vertically incident cosmic muon can have a track length of up to 80 cm, compared to no more than 53 cm for a horizontal (beamline) track. This then allows for a broader characterisation of the detector response.

5.2 Operational Configuration

The ARIADNE detector was operational 24 hours a day for the duration of cosmic muons data-taking, in order to maximise the live time and record as many events as possible. As noted above, a longer event window - of 1 ms length - was possible due to relatively low rate of cosmic muon pileup.

As previously noted, the monolithic THGEM, discussed in Section 2.3, was used for cosmic muons data-taking, and the DAQ and trigger system was set up and operated exactly as described in Section 3.2 and Figure 31. It was found that water-cooling the EMCCD cameras to a temperature of -80°C did not result in an appreciable reduction in the background per-pixel intensity when compared to air-cooling to -70°C, and so the latter was used for cosmic muon operation.

Table 3 shows the various parameters that were used during cosmic muon operation, arranged by device.

5.3 Results

Figure 40 presents a selection of cosmic muon events as captured by the ARIADNE detector using an EMCCD image binning of 4×4 pixels, an EMCCD gain of 1000, and a THGEM field of 30 kV/cm. The PMT signals and EMCCD images are correlated, and the S1 and S2 pulses can be clearly identified on the former.

Figure 40 (top) represents a cosmic muon that entered the TPC from the top, passing through the THGEM itself. This can be inferred from the fact that the S1 and S2 pulses on the PMT signal have no separation in time - meaning that the electrons at the start of the ionisation track travelled effectively zero distance in the z direction between their initial position and the THGEM. However, it is evident that this particle did not pass vertically through the TPC, but rather at an angle: if it

Parameter	Value	Comments
EMCCDs		
Gain	Variable	Up to the maximum available value of 1000
Cooling	Air	Allows operating temperature of -70°C, reducing the background per-pixel intensity to $\approx$ 500 ADU
Binning	Variable	
Exposure Time	1 ms	
PMTs		
Biases	970V 1100V 1300V 950V	Different voltages used so as to equalise the individual PMT responses
Recording Length	250,000 datapoints	Gives an event window of 1 ms, consistent with EMCCDs
Field Cage Biases		
Cathode	-46.0 kV	Nominal drift field of 540 V/cm
Extraction Grid	-3.0 kV	
THGEM Top	Variable	Between +1.0 to +2.2 kV
THGEM Bottom	-1.0 kV	
Other		
Cryostat pressure	1.08 bar	

Table 3: Operational parameters for the ARIADNE detector taking cosmic muon data at the University of Liverpool.

had been completely vertical, the corresponding track would have a very short $x - y$ projection, but the EMCCD image shows an $\approx$ 55 cm long track.

Figure 40 (middle) shows an electromagnetic shower, possibly originating from a γ, as is indicated by the lack of an ionisation track leading to the primary vertex. A number of daughter products, both charged and uncharged, can be seen and/or inferred from the shape and position of the tracks as the shower develops. The PMT signal indicates that the originating γ entered the active volume from the side - assuming a high purity and therefore a drift velocity of 1.5 mm/μs, the gap of $\approx$ 103 μs between the S1 and S2 pulses would correspond to a z distance of $\approx$ 15.5 cm below the THGEM. The S2 pulse itself exhibits more internal structure than that in the top image, due to the numerous tracks within the shower.

Figure 40 (bottom) also depicts a cosmic muon that entered the active TPC volume from the top, with the S1 and S2 PMT pulses being correspondingly separated by zero time. However, in comparison to the top image, the EMCCD track is somewhat shorter at $\approx$ 30 cm, but the S2 pulse is longer - lasting $\approx$ 450 μs compared to the 250 μs duration S2 pulse in the top image. Together, these indicate that the muon in the bottom image travelled at a steeper angle through the TPC than the muon in the top image.
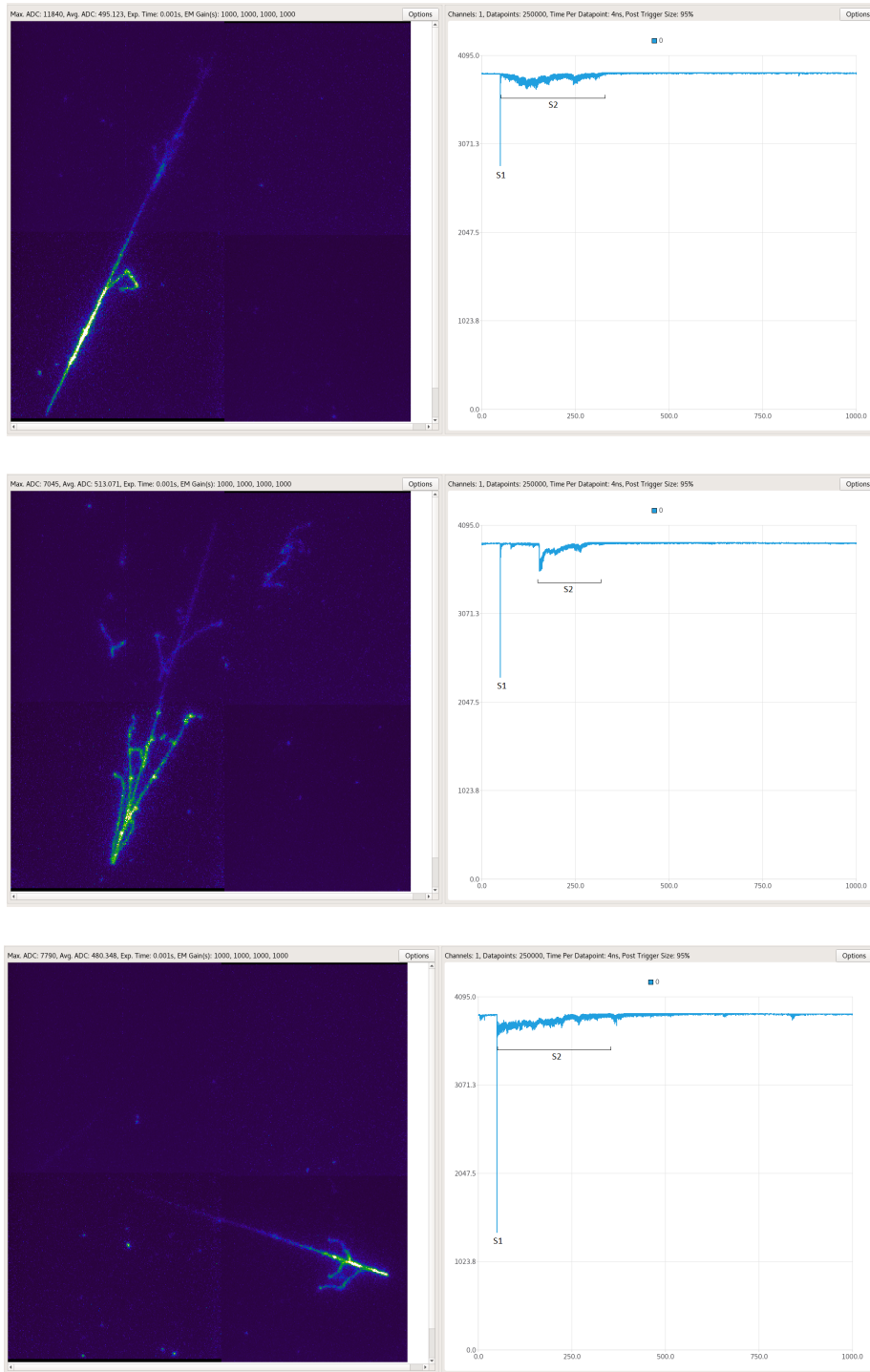
Figure 40: A selection of cosmic muon events as captured by the ARIADNE detector - the maximum intensities are (from top to bottom) 11840, 7045 and 7790 ADU. The EMCCD images and PMT signals are correlated within each event, and the S1 and S2 pulses are labelled on the PMT signals.

Figure 41 shows cosmic muons recorded using three different EMCCD binning scenarios: 4×4, 8×8 and 16×16. The left image is the same as that shown in Figure 40 (top), and has been reproduced here for comparison to the others. As a reminder of the calculation performed in Section 3.4, the spatial resolution of the images are 1.1, 2.2 and 4.4 mm/pixel respectively.
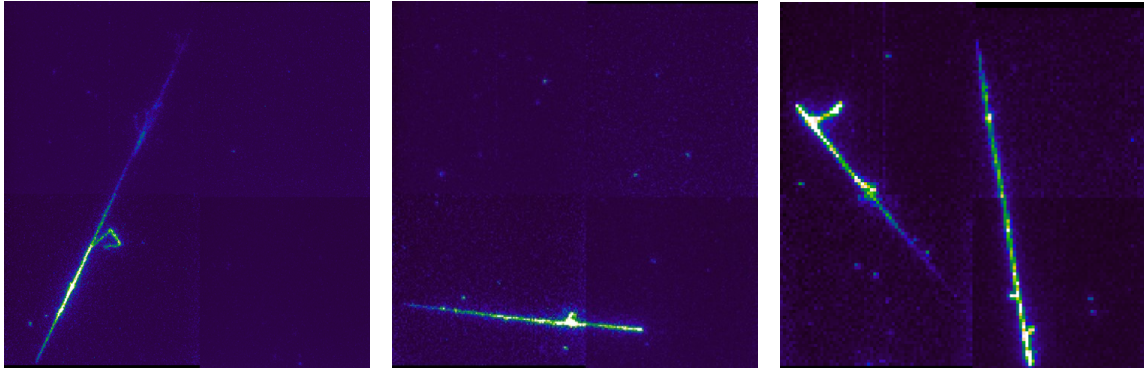

Figure 41: A selection of cosmic muon events as captured by the ARIADNE detector at different EMCCD binnings: (left) 4×4, (middle) 8×8, and (right) 16×16.

It can be seen that even 16×16 binning produces very clearly defined particle tracks, with an image resolution of 4.4 mm/pixel as noted in Section 3.4 above. As previously discussed in Section 4.4, this image resolution is only a part of the overall detector spatial resolution: a large LArTPC of 12 m drift length operating at a drift field of 0.5 kV/cm would experience a transverse electron diffusion of up to ≈ 4.2 mm - effectively an equal contribution to the detector spatial resolution to that from the image resolution at 16×16 binning.

Although operating the EMCCDs at finer binning reduces their contribution to the overall detector resolution, using a coarser binning has advantages for data rates and sizes - the readout rate of the EMCCDs increases approximately linearly with binning "coarseness" [10], and file sizes are directly related to the number of post-binning pixels to be read out. Coarser binning also increases the overall light collection per pixel, reducing statistical effects that might otherwise have an impact on intensity and energy analysis, particularly for incident particles at low momenta.

The monolithic THGEM was able to operate stably at a higher field than the segmented one, reaching up to 32 kV/cm before discharges (previously discussed in Section 2.3) made further increase untenable. This increased stability is due to the simpler, single-channel design: with only a single bias required for the top plane instead of 16, there is less possibility for defects such as that which affected the operation of the segmented THGEM.

Stable operation allowed the characterisation of the relative light yield of the THGEM as a function of the field across it - quantified by dI, the summed intensity of all pixels along a given track on the EMCCD image. This value not exactly the same as the THGEM gain, but is related to it (both being functions of the number of electrons leaving the THGEM holes) and so can still be used an reasonable indicator.
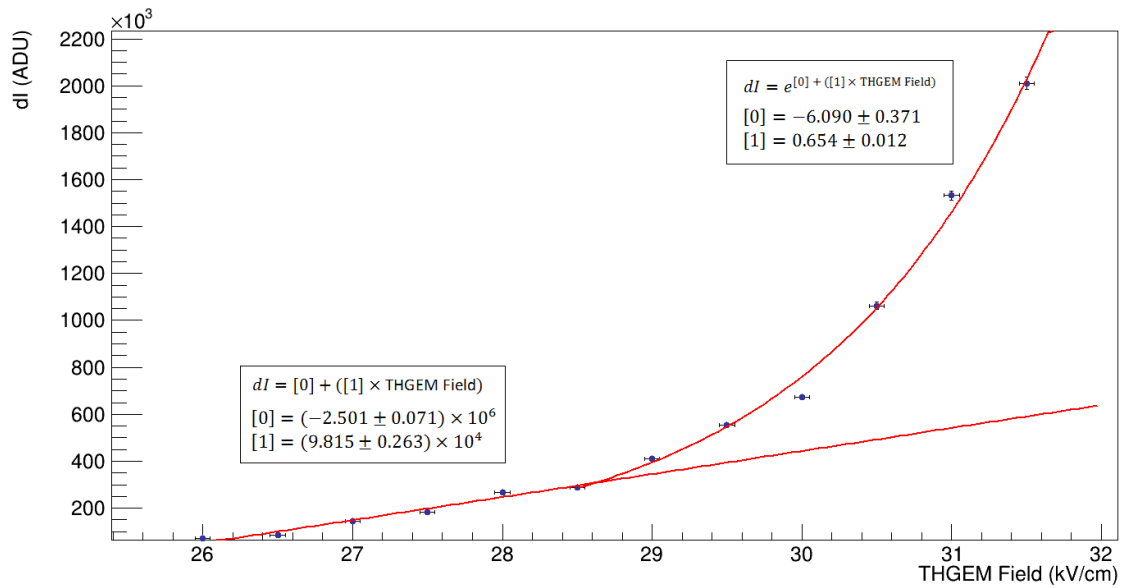
Figure 42a shows the relation between the THGEM field and *dI*, for cosmic muons which pass through both the THGEM and the cathode grid, recorded with an EMCCD image binning of 4 × 4 and EMCCD gain of 1000. Cosmic muons - being minimum ionising particles (MIPs) - have a specific energy loss of ≈ 2.1 MeV/cm in LAr [35], and so this relation also represents the energy calibration of the detector at these EMCCD settings. Figure 42b shows the same relation under the same selection of muons, but now for an EMCCD image binning of 8 × 8 and EMCCD gain of 500. A lower gain was required for the coarser binning due to the previously noted increased light collection per pixel, which was seen to result in saturation if an EMCCD gain of 1000 was used at 8 × 8 binning.

In the 4 × 4 binning scenario, it can be seen that there is a linear relationship below a field of ≈ 28.5 kV/cm, corresponding to the low-bias, no-gain regime in which the drift electrons simply pass through the THGEM holes and collect on the top plane. However, as the field increases beyond 28.5 kV/cm, the value of *dI* now increases in an exponential fashion, indicating the electron multiplication regime.

The turn-over field value between the two regimes is effectively identical for the 8 × 8 binning scenario - as expected, since it is a function of the THGEM, and should therefore be unaffected by any changes in the EMCCD operating parameters.
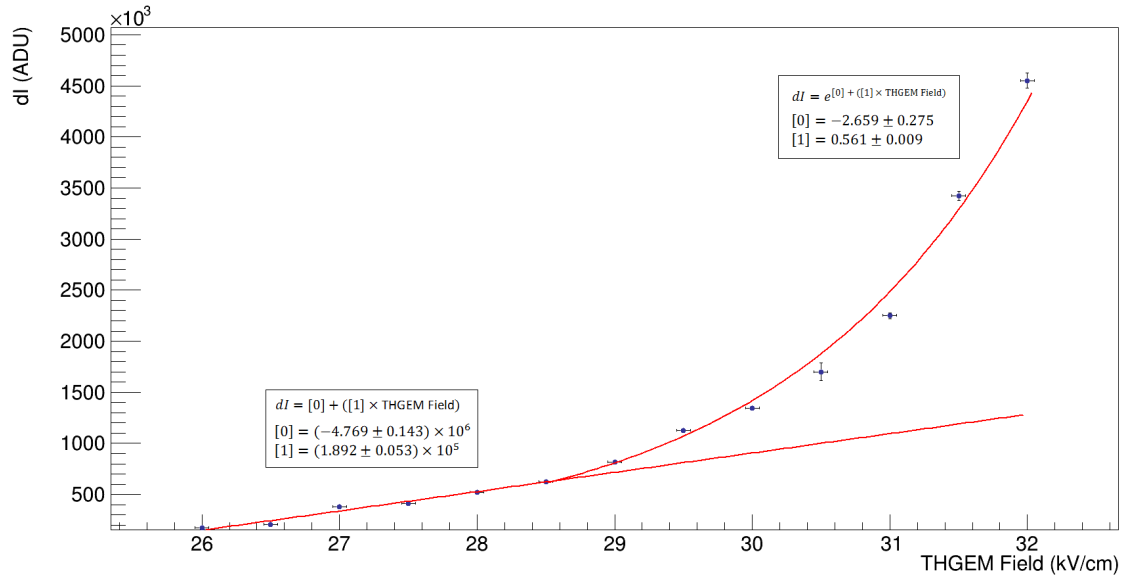
(a) EMCCD image binning of 4×4 and EMCCD gain of 1000

(b) EMCCD image binning of 8×8 and EMCCD gain of 500

Figure 42: The relation between the total charge dI - the summed intensity of all EMCCD pixels along a track - and the THGEM field. Each datapoint is the fitted Landau MPV of all single-track dI values at that THGEM field, and the displayed errors bars are the error on each MPV (y-axis) and the uncertainty in the total THGEM field (x-axis) due to the precision of the power supply. In both scenarios, only those cosmic muons which passed through both the THGEM and cathode grids were used, and linear and exponential functions have been fitted to the six lowest and highest datapoints respectively (with fit parameters as shown). Both functions are drawn extended to highlight the cross-over point between the no-gain and electron-multiplying regimes.

6 Summary and Outlook

The main aim of the ARIADNE experiment is to demonstrate the concept of an optical readout method for two-phase LArTPC particle detectors - making use of the secondary scintillation light that is naturally produced in the THGEM of a two-phase TPC. An optical readout could have considerable advantages over traditionally-used charge readouts - including better energy and position sensitivity, and massive simplification of construction, operation and upgrading, together with corresponding reductions in costs - all of which are important to consider as colossal-scale experiments, such as the four 17 kiloton DUNE LArTPCs, move from concept to reality.

ARIADNE utilises 4 single-photon sensitive EMCCD cameras to view the $x - y$ projection of secondary scintillation light produced by a 53×53 cm THGEM operating in concert with a TPC of drift length 80 cm. PMTs capture both the prompt and secondary scintillation light, allowing for measurements of the z axis projection, and therefore - with correlation to the EMCCDs - full 3D reconstruction of particle tracks.

The ARIADNE detector was operated at the CERN T9 testbeam between March and April 2018, in order to characterise the detector hardware with a controlled, well-described source of mixed particles over a range of momenta. The results - which constitute the first ever optical images of beamline interactions in a two-phase LArTPC - demonstrate the high signal-to-background ratio that naturally comes from the use of the secondary scintillation light, and that the optical readout method is sensitive enough to identify particle tracks even with little or no THGEM gain. Full 3D track reconstruction and analysis is ongoing, but has proved challenging due to particle pileup within the acquisition window (primarily caused by "halo" muons produced at the T9 source).

Further operation was conducted at the University of Liverpool using cosmic muons, along with certain upgrades to the detector hardware as informed by CERN operation. A simpler THGEM design allowed for more stable running at higher fields, and the low-gain and electron-multiplying regimes have been successfully demonstrated. A study on varying the EMCCD image binning indicates that even at the lowest possible spatial resolution of 4.4 mm/pixel, particle tracks are still clearly identifiable, with this coarser binning having additional operational advantages such as a faster acquisition rate, reduced data size and increased light collection per pixel.

Work is ongoing to further develop optical TPC data analysis software. In particular, the pixel-based nature of optical readout is well-suited to the use of neural networks and other forms of machine learning, which could result in extremely high-efficiency PID and event classification.

Although the EMCCDs used thus far have successfully proved the feasibility of optical readout, there are a number of avenues for future R&D to improve the performance of readout devices. Of particular interest is the development of camera technologies which offer extremely high-rate data acquisition and/or high-precision time-stamping, allowing for 3D particle track reconstruction without the need for correlation to PMTs. One such technology - a Timepix3-based camera - has recently been demonstrated for optical readout in a low pressure CF_4 TPC [36], and is to be used as an upgrade to the ARIADNE detector in the near future. Other studies will also investigate increasing the stability and electroluminescence yield of THGEMs, possibly including the development of new THGEM designs which are specifically optimised for light - rather than charge - production.

Acknowledgments

References

[1] R. Acciarri et al., Long-Baseline Neutrino Facility (LBNF) and Deep Underground Neutrino Experiment (DUNE) Conceptual Design Report Volume 1: The LBNF and DUNE Projects, arXiv:1601.05471 [physics.ins-det]

[2] C. E. Aalseth et al., DarkSide-20k: A 20 Tonne Two-Phase LAr TPC for Direct Dark Matter Detection at LNGS, arXiv:1707.08145 [physics.ins-det]

[3] K. Mavrokoridis et al., Optical Readout of a Two Phase Liquid Argon TPC using CCD Camera and THGEMs, arXiv:1401.0525 [physics.ins-det]

[4] K. Mavrokoridis et al., First Demonstration of Imaging Cosmic Muons in a Two-Phase Liquid Argon TPC using an EMCCD Camera and a THGEM, arXiv:1507.06586 [physics.ins-det]

[5] COMSOL Multiphysics Modeling Software, https://uk.comsol.com/ (Accessed: 2018/11/09)

[6] Heinzinger - Universal high-voltage power supplies PNC up to 300,000 Volt with superb precision, https://www.heinzinger.de/fileadmin/user_upload/Datenblaetter/en/Universal-High-Voltage-Power-supplies-PNC-heinzinger.pdf (Accessed: 2018/09/18)

[7] A. Breskin et al., A concise review on THGEM detectors, Nucl. Instrum. Meth. A, Volume 598, Issue 1 (2009), Pages 107-111

[8] C. M. B. Monteiro et al., Secondary scintillation yield from GEM and THGEM gaseous electron multipliers for direct dark matter search, Physics Letters B, Volume 714, Issue 1 (2012), Pages 18-23

[9] Hamamatsu - Large Photocathode Area Photomultipler Tubes, https://www.hamamatsu.com/resources/pdf/etd/LARGE_AREA_PMT_TPMH1286E.pdf (Accessed: 2018/09/18)

[10] Andor - iXon Ultra 888 Specifications, http://www.andor.com/pdfs/specifications/iXon_Ultra_888_EMCCD_Specifications.pdf (Accessed: 2018/09/18)

[11] V. M. Gehman et al., Fluorescence efficiency and visible re-emission spectrum of tetraphenyl butadiene films at extreme ultraviolet wavelengths, Nucl. Instrum. Meth. A, Volume 654, Issue 1 (2011), Pages 116-121

[12] B. Broerman et al., Application of the TPB Wavelength Shifter to the DEAP-3600 Spherical Acrylic Vessel Inner Surface, Journal of Instrumentation, Volume 12, Issue 4 (2017), Page P04017

[13] M. Spanu et al., Study on TPB as wavelength shifter for the new ICARUS T600 light collection system in the SBN program, Journal of Physics: Conference Series, Volume 956 (2018), Page 012016

[14] The ArDM Collaboration, Development of wavelength shifter coated reflectors for the ArDM argon dark matter detector, Journal of Instrumentation, Volume 4, Issue 6 (2009), Page P06001

[15] M. N. Spanu (on behalf of ICARUS/WA104 collaborations), TPB thickness and Quantum Efficiency measurements for the new ICARUS T600 light detection system in the SBN program, Journal of Physics: Conference Series, Volume 888 (2017), Page 012092

[16] E. Buckley et al., A Study of ionization electrons drifting over large distances in liquid argon, Nucl. Instrum. Meth. A, Volume 275, Issue 2 (1989), Pages 364-372

[17] G. Carugno et al., Electron lifetime detector for liquid argon, Nucl. Instrum. Meth. A, Volume 292, Issue 3 (1990), Pages 580-584

[18] W. Walkowiak, Drift velocity of free electrons in liquid argon, Nucl. Instrum. Meth. A, Volume 449, Issues 1-2 (2000), Pages 288-294

[19] M. J. Carvalho and G. Klein, Luminescence decay in condensed argon under high energy excitation, Journal of Luminescence, Volume 18-19, Part 1 (1979), Pages 487-490

[20] A. Hitachi et al., Effect of ionization density on the time dependence of luminescence from liquid argon and xenon, Physical Review B, Volume 27, Issue 9 (1983), Pages 5279-5285

[21] C. Amsler et al., Luminescence quenching of the triplet excimer state by air traces in gaseous argon, Journal of Instrumentation, Volume 3, Issue 2 (2008), Page P02001

[22] K. Mavrokoridis et al., Argon Purification Studies and a Novel Liquid Argon Re-circulation System, arXiv:1106.5226 [physics.ins-det]

[23] Baumer - Ultrasonic distance measuring sensors, https://www.baumer.com/gb/en/product-overview/distance-measurement/ultrasonic-distance-sensors/u500-da0-aa1b-72o/p/medias/__secure__/U500_DA0_AA1B_7200_0000_web_EN.pdf?mediaPK=8800546979870 (Accessed: 2018/12/27)

[24] Cryomech - AL300 Cryocoolers, https://www.cryomech.com/products/al300/ (Accessed: 2018/07/13)

[25] A. Ereditato et al., Measurement of the drift field in the ARGONTUBE LAr TPC with 266 nm pulsed laser beams, Journal of Instrumentation, Volume 9, Issue 11 (2014), Page P11010

[26] B. Rossi (on behalf of LHEP liquid Argon group), Monitoring the parameters of a large size liquid Argon Time Projection Chamber using UV laser beams, Journal of Physics: Conference Series, Volume 308 (2011), Page 012025

[27] Quantel - Q-Smart 100 Specifications, http://www.quantel-laser.com/tl_files/client/MYQUANTELSPACE/SalesLiterature/Q-smart100_Specs_EN_012014.pdf (Accessed: 2018/11/18)

[28] PAR Group Ltd. - Viton® Rubber Sheeting - Grade "A" Technical Data Sheet https://www.par-group.co.uk/site-content/1/Docs/updates/2-sealing-and-jointing/2.41.1-viton-rubber-sheeting-grade-a-tds.pdf (Accessed: 2018/01/16)

[29] A. Blatter et al., Experimental study of electric breakdowns in liquid argon at centimeter scale, Journal of Instrumentation, Volume 9, Issue 4 (2014), Page P04006

[30] CERN - East Area Documentation,
http://sba.web.cern.ch/sba/BeamsAndAreas/East/East.htm (Accessed: 2017/10/09)

[31] Y. Li et al., Measurement of longitudinal electron diffusion in liquid argon, Nucl. Instrum. Meth. A,
Volume 816 (2016), Pages 160-170

[32] K. T. McDonald, Electron Diffusion in Liquid Argon (presented at the MicroBooNE 2009
Collaboration Meeting),
http://www.hep.princeton.edu/~mcdonald/microBooNE/KTM/diffusion_constant.pdf
(Accessed: 2019/06/15)

[33] R. Acciarri et al., Long-Baseline Neutrino Facility (LBNF) and Deep Underground Neutrino
Experiment (DUNE) Conceptual Design Report, Volume 4 The DUNE Detectors at LBNF,
arXiv:1601.02984 [physics.ins-det]

[34] M. Tanabashi et al. (Particle Data Group), Review of Particle Physics, Phys. Rev. D Volume 98, Issue
3 (2018), Page 030001

[35] Liquid Argon Properties (Tables and Calculators),
https://lar.bnl.gov/properties/#particle-pass (Accessed: 2019/05/14)

[36] A. Roberts et al., First demonstration of 3D optical readout of a TPC using a single photon sensitive
Timepix3 based camera, Journal of Instrumentation, Volume 14, Issue 6 (2019), Page P06001